Thermosphere-Ionosphere Modeling With Forecastable Inputs: Case Study of the June 2012 High Speed Stream Geomagnetic Storm

Xing Meng[1], Anthony J. Mannucci[1], Olga P. Verkhoglyadova[1], Bruce T. Tsurutani[1], Aaron J. Ridley[2], and Ja-Soon Shim[3]

[1]Jet Propulsion Laboratory, California Institute of Technology, Pasadena, CA, USA
[2]Department of Climate and Space Sciences and Engineering, University of Michigan, Ann Arbor, MI, USA
[3]Catholic University of America, NASA GSFC, Greenbelt, MD, USA

Key Points:

- Forecastable global thermosphere-ionosphere modeling is carried out for a weak geomagentic storm.
- The modeled daytime middle-low-latitude TEC response is primarily driven by the solar wind condition on the first day of the storm.
- On later days of the storm the solar irradiance plays a comparable role as the solar wind in determining the modeled daytime TEC response.

This is the author manuscript accepted for publication and has undergone full peer review but has not been through the copyediting, typesetting, pagination and proofreading process, which may lead to differences between this version and the Version of Record. Please cite this article as doi: 10.1029/2019SW002352

Corresponding author: Xing Meng, Xing.Meng@jpl.nasa.gov

Abstract

Forecasting conditions in the thermosphere and ionosphere is a key outcome expected from space weather research. In this work, we perform numerical simulations using the first-principles models Global Ionosphere Thermosphere Model (GITM) and Thermosphere Ionosphere Electrodynamics General Circulation Model (TIE-GCM) to address the reliability of thermospheric-ionospheric forecasts. When considering forecasts applicable to periods of geomagnetic activity, careful consideration is required of model inputs, which largely determine how the models will simulate disturbed conditions. We adopt an approach to drive the models with solar wind parameters and the 10.7 cm solar radio flux. This aligns our investigation with recent research and operational activities to forecast solar wind conditions at the Earth a few days in advance. In this work, we examine a weak geomagnetic storm, the June 2012 high-speed-stream event, for which we drive GITM and TIE-GCM with observed solar wind and F10.7 values. We find general agreement between the simulations and observation-based Global Ionospheric Maps of the total electron content (TEC) response. However, overestimated TEC response is found in the middle-low latitudinal region of the American sector and surrounding areas for both GITM and TIE-GCM during similar time periods. By conducting numerical modeling experiments and comparing the modeling results with observational data, we find that the overestimated TEC response can be almost equally attributed to the solar wind driving and F10.7 driving during the June 2012 event. We conclude that the accuracy of the high-latitude electric field and the solar irradiance are crucial to reproduce the TEC response in forecastable-mode modeling.

1 Introduction

As a component of space weather, the terrestrial thermospheric and ionospheric responses to the varying conditions on the Sun and in interplanetary space have been extensively studied. These studies provide not only improved understanding of the thermosphere-ionosphere system but also create the possibility of forecasting conditions in the upper atmosphere with lead times extending to a few days. As of today, research into forecasting thermospheric and ionospheric conditions can be achieved with numerical models of the upper atmosphere, including data-assimilative models and fully physics-based models [*Keil*, 2007; *Schunk et al.*, 2005, 2012, 2014; *Mannucci et al.*, 2015]. Data-assimilative models have been used for short-term (a few hours) forecasts [*Schunk et al.*, 2004; *Mat-*

suo et al., 2013; *Chartier et al.*, 2016; *Chen et al.*, 2016]. To achieve forecasts with a-few-day lead times, one must forecast the solar drivers that strongly influence the thermospheric and ionospheric response to geomagnetic disturbances. Fortunately, fully physics-based models [*Richmond et al.*, 1992; *Roble and Ridley*, 1994; *Millward et al.*, 1996; *Huba et al.*, 2000; *Ridley et al.*, 2006] are able to accept such drivers as input, and thus can in principle be used for a-few-day lead time forecasts as long as forecasted solar drivers are available. While this research area is still in its early stages, solar wind and solar irradiance forecasts are major focuses of the space weather research effort [*Owens et al.*, 2008; *Jian et al.*, 2015; *Henney et al.*, 2015; *Warren et al.*, 2017]. Therefore, we investigate thermospheric-ionospheric forecasts with a lead time of a few days from the perspective that reliable solar forecasts will eventually be available a few days ahead. We refer to forecasts with a-few-day lead time as "medium range" forecasts in the rest of the paper.

The quantity of research on medium range forecasting of the thermosphere-ionosphere system is at present somewhat limited [*Mannucci et al.*, 2016; *Shim et al.*, 2017]. To gain a quantitative understanding of how accurate a medium range thermospheric-ionospheric forecast might be, we perform simulations with fully physics-based models, using inputs that can be derived from medium range solar wind and solar irradiance forecasts. The models will not produce a perfect forecast even if the medium range drivers are forecasted perfectly. This aspect of forecast error is our primary focus in this paper. We defer to future work the assessment of thermospheric-ionospheric forecasts that are driven by imperfect solar wind and solar irradiance forecasts. *Meng et al.* [2016] reports our initial attempt to formulate ionospheric total electron content (TEC) forecasting with the fully physics-based Global Ionosphere-Thermosphere Model (GITM) and address its forecasting performance across multiple geomagnetic storms caused by high-speed solar wind streams. That study analyzed a specific case of a forecast missing an observed TEC change. A detailed analysis was performed of the different terms leading to electron density changes in the model, but a dominant cause of the forecast error was not determined. In this paper, we present a detailed examination of a case when the forecasts from the physics-based models, GITM and Thermosphere Ionosphere Electrodynamics General Circulation Model (TIE-GCM) both significantly overestimate an observed TEC change during the June 2012 high-speed-stream storm and perform modeling experiments to identify the causes of the overestimation.

For this study, GITM and TIE-GCM are driven solely by the solar wind conditions (interplanetary magnetic field data included) measured upstream of the magntosphere and the 10.7 cm solar radio flux (F10.7 flux). We consider our model runs to be medium range "forecastable-mode" modeling in the sense that, were solar wind and F10.7 flux inputs available a few days ahead, the models would produce medium range forecasts. Typically, GITM and TIEGCM simulations are conducted with inputs that are not available in advance, such as the auroral hemispheric power index and solar irradiance data based on satellite measurements. Several studies in the literature have performed model runs using inputs based on observations from ground magnetometers and radars along with satellites [e.g., *Shiokawa et al.*, 2007; *Lu et al.*, 2015; *Verkhoglyadova et al.*, 2016]. Currently there is no proposed method to forecast such observations, so analyzing model runs based on inputs derived from these observations does not directly address quantitative assessment of medium range thermospheric-ionospheric forecasts. Instead, we expect medium range forecasts of the near-Earth solar wind and F10.7 flux to be used in thermospheric-ionospheric forecasts. The F10.7 flux input for GITM and TIE-GCM "forecastable-mode" modeling consists of daily F10.7 flux and 81-day center-averaged F10.7 flux. The medium range forecast of 81-day center-averaged F10.7 flux requires a forecast of daily F10.7 flux at least 40 days in advance. The 45-day forecast of daily F10.7 flux is available at the Space Weather Prediction Center (`https://www.swpc.noaa.gov/products/usaf-45-day-ap-and-f107cm-flux-forecast`) and has also been constructed by *Warren et al.* [2017].

The following content of the paper has four parts. Section 2 describes the June 2012 storm event, the forecastable-mode inputs for GITM and TIE-GCM, as well as the modeling experiments. Section 3 presents results from the modeling experiments. Section 4 discusses the implications of the results for future thermospheric-ionospheric forecasts. Section 5 concludes the paper.

2 Methodology

2.1 Event Description

The June 2012 geomagnetic storm is a weak event driven by a high-speed solar wind stream. The solar wind and geomagnetic conditions from the OMNI 1-minute resolution data (http://omniweb.gsfc.nasa.gov) are depicted as the black lines in Figure 1 (The

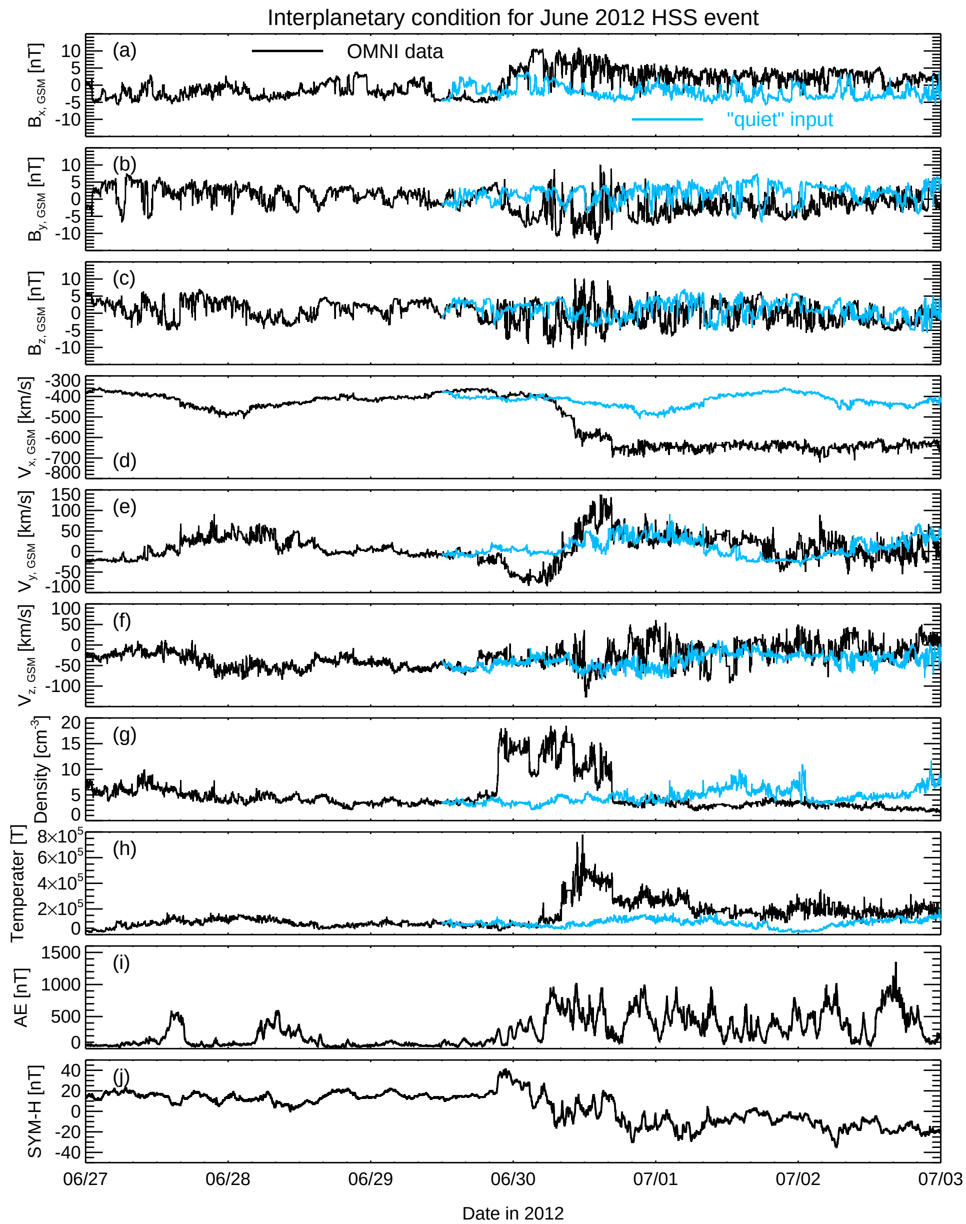

108 **Figure 1.** The interplanetary conditions and geomagnetic activity indices for the June 2012 event from the OMNI data (black) and constructed quiet solar wind (blue). The interplanetary conditions from OMNI are input to the original forecastable-mode GITM and TIE-GCM runs, while the quiet solar wind is used to drive modeling experiments 1 and 3 (see below).

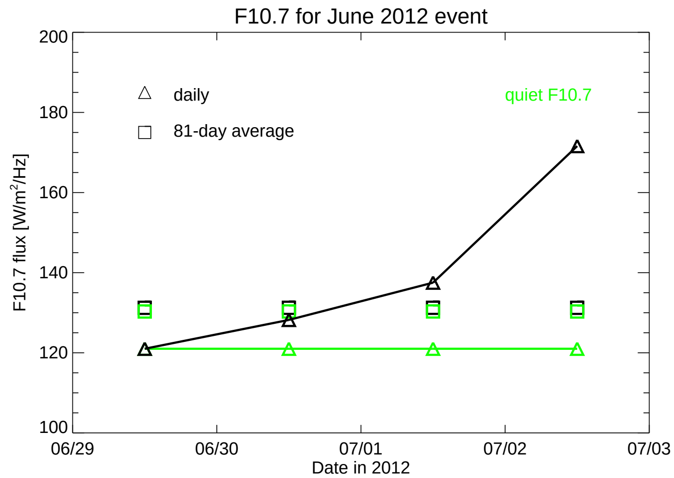

Figure 2. The daily (triangles) and 81-day center-averaged (squares) F10.7 solar flux indices for the June 2012 event. The actual values (black) are used to drive the original forecastable-mode GITM and TIE-GCM runs, while the constructed quiet values (green) are for modeling experiments 2 and 3 (see below).

blue lines are used in a modeling experiment and are described later). The solar wind corotating interaction region (CIR) encountered Earth during the final hour of June 29 and lasted for more than 12 hours. During this time period, the interplanetary magnetic field oscillated up to +/- 10 nT along the y and z directions in the Geocentric Solar Magnetospheric (GSM) coordinate system (panels (b) and (c) of Figure 1). The solar wind speed climbed from about 400 km/s to nearly 700 km/s (panel (d)). The density and temperature increases (panels (g) and (h)) are typical solar wind features during CIR passages [*Tsurutani et al.*, 2006]. The geomagnetic activity indices showed mild disturbances: the AE index rarely exceeded 1000 nT (panel (i)); the minimum SYM-H index was -35 nT (panel (j)), and therefore this is a weak storm [*Gonzalez et al.*, 1994]. According to the SYM-H index, the weak storm started at the end of June 29 and lasted for several days, at least until July 3.

This event is under a special condition that the F10.7 flux increased rapidly and continuously before and during the storm days. The daily F10.7 flux, represented by the black triangles in Figure 2, increased from 120 $W/m^2/Hz$ to above 170 $W/m^2/Hz$ from June 29 to July 2. In fact, although not shown in this figure, the daily F10.7 flux started to increase several days prior to June 29. This continuous increase was due to a few active regions on the Sun rotating into view. The event offers a special case when the thermosphere-ionosphere system is exposed to both storm-inducing interplanetary structures and significant solar irradiance variations. With the help of controlled numerical modeling experiments, one could possibly isolate and identify the ionospheric response to each of the two drivers.

2.2 GIM Data Description

We use Global Ionosphere Maps (GIM) from JPL [*Mannucci et al.*, 1998] as a reference to compare the forecastable-mode modeling results to. The GIM provides interpolated total electron content (TEC) from a global ground network of Global Positioning System (GPS) receivers and is found to be an accurate representations of the vertical ionospheric TEC particularly over continents where GPS ground receivers are ample [*Hernandez-Pajares et al.*, 2009; *Yasyukevich et al.*, 2010]. Comparisons between the GIM TEC and independent TEC measurements from the TOPEX altimeter have shown that the GIM algorithm is accurate up to 2000 km from a reference ground GPS station. In particular, the difference between the GIM TEC and the TOPEX TEC is less than 1.5 TECU for regions within 1500 km from a ground GPS station [*Ho et al.*, 1997; *Iijima et al.*, 1999]. The accuracy of GIM TEC reduces with the increasing distance from a GPS ground station.

Figure 3 shows the locations of the ground GPS stations (red dots) over the American sector. These were the stations from which the data were collected and used to obtain the GIM during the focused period of this study (This particular map applies to July 1, 2012 but is applicable to other days during late June and early July of 2012 as well). The green rectangle represents the local region of interest, for which we will analyze the TEC and compare to the TEC from the forecastable-mode modeling. This local region, 85°W - 65°W and 45°S - 25°S, is filled by a number of GPS ground stations, and the distances from these stations to the margins of the local region fall within 1500 km. Therefore, we expect that the GIM TEC accuracy in the local region is sufficient to support the conclusions in this study. The vertical green line marks the geographic longitude of 75°W, where we will extract a meridional cut from GIM TEC a nd compare it to the forecastable-mode modeling resutls. Since there are almost always stations within 1500 km along the 75°W

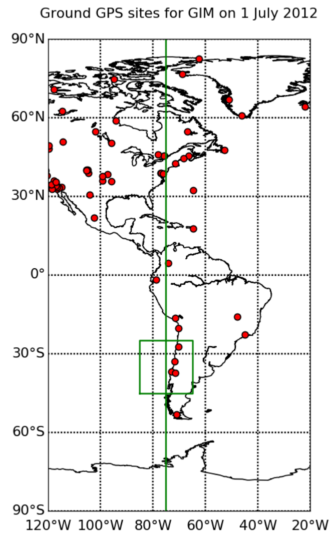

Figure 3. GPS sites (red dots) over the American sector used for generating the GIM TEC on July 1, 2012. The vertical green line represents geographic longitude 75°W. The green rectangle represents the geographic region of 85°W - 65°W, 45°S - 25°S.

meridian, except for the high-latitude region in the southern hemisphere, we expect that the GIM TEC along 75°W is accurate to use as a reference TEC.

2.3 Forecastable-mode Modeling Description

We conducted forecastable-mode ionospheric modeling for the June 2012 event with two state-of-the-art models: Global Ionosphere-Thermosphere Model (GITM) [*Ridley et al.*, 2006] and Thermosphere Ionosphere Electrodynamics General Circulation Model (TIE-GCM) [*Richmond et al.*, 1992; *Roble and Ridley*, 1994].

GITM is a three-dimensional physics-based model that solves for the non-hydrostatic continuity, momentum, and energy equations for the upper atmosphere between around 100 km and 600 km altitudes. The computational grid is a flexible Cartesian grid based on geographic longitude, latitude, and altitude. The initial and lower boundary conditions, including neutral densities, temperature and velocities, are defined by empirical models Mass Spectrometer and Incoherent Scatter (MSIS) [*Hedin*, 1991] and Horizontal Wind Model (HWM) [*Drob et al.*, 2008]. GITM has several options of specifying the solar irradiance, the high-latitude electric field, and the auroral particle precipitation. For a forecastable-mode simulation, we require that the model inputs are all forecastable in the sense that they can be derived from a forecast of the solar wind upstream of the magnetosphere, and the F10.7 flux. Therefore, we drive GITM with 1) the solar wind data at 1 AU, which provides the high-latitude electric field via the Weimer empirical model [*Weimer*, 2005a,b] and the auroral particle precipitation pattern via the OVATION (Oval Variation, Assessment, Tracking, Intensity, and Online Nowcasting) Prime model [*Newell et al.*, 2009], and 2) the daily and 81-day center-averaged F10.7 indices, which provides the solar irradiance primarily via empirical models EUVAC [*Richards et al.*, 1994], Tobiska91 [*Tobiska*, 1991], Hinteregger [*Hinteregger*, 1981], and Woods and Rottman [*Woods and Rottman*, 2002] for different wavelength channels. The grid resolution for the forecastable-mode GITM run is set to be 3.3° in longitude, 1° in latitude, and 1/3 of the local scale height in the vertical direction.

TIE-GCM [*Qian et al.*, 2014; *Maute*, 2017] is another three-dimensional physics-based model of the upper atmosphere. It has similar core equations and boundary conditions as GITM, but it is also different from GITM in many aspects. A significant difference is that TIE-GCM assumes hydrostatic equilibrium while GITM does not. Other differences include: the computation of middle-low latitude electrodynamics, vertical grid setting and spacing, numerical scheme, etc. Similar to GITM, TIE-GCM can be driven by various options for specifying the solar irradiance [*Qian et al.*, 2008; *Solomon et al.*, 2011], the high-latitude electric field, and the auroral particle precipitation. For a forecastable-mode TIE-GCM simulation, we drive the model with the same inputs as for GITM: the solar wind at 1 AU as well as daily and 81-day center-averaged F10.7 indices. The solar wind inputs are used by the Weimer model to provide the high-latitude electric field [*Solomon et al.*, 2012], and the F10.7 indices are used to specify the solar irradiance via empirical models [*Solomon and Qian*, 2005]. Unlike GITM, the auroral particle precipitation is computed based on the hemispheric power, which is based on an empirical relationship using the interplanetary magnetic field and the solar wind velocity [*Emery et al.*, 2008]. The forecastable-mode TIE-GCM run uses Version 2.0 of TIEGCM, and the horizontal grid resolution is set to be 5° in both longitude and latitude.

To evaluate the storm-time TEC response to the June 2012 event, we identify June 29 as the pre-storm day or quiet day, with a daily Ap index of 5. The forecastable-mode GITM simulation begins on June 21 and ends on July 2, with the first eight days as a "warm up" period. The forecastable-mode TIE-GCM simulation was carried out at the

Community Coordinated Modeling Center, and it had a 20-day "warm up" period as a convention. The "warm up" period, for either GITM or TIE-GCM, is to stabilize the model solution over a course of multiple days. The model solutions from GITM and TIE-GCM at the end of their "warm up" periods were examined to make sure that the solutions are stable. The simulated quiet-time baseline TEC is subtracted from the simulated storm-time TEC to obtain the difference TEC, which represents the ionospheric response to the storm event. Figure 4 displays global maps of the TEC at 18UT on the quiet day June 29, at 18UT on the second day of the storm, July 1, and the difference TEC obtained by subtracting the quiet-time TEC shown in the left column from the storm-time TEC shown in the middle column. The TEC maps from GITM, TIE-GCM, and GIM are displayed in three rows from top to bottom, respectively. Overall, the TEC values from GITM and TIE-GCM share similarities with GIM TEC. However, both GITM and TIE-GCM produce a significant TEC enhancement over the south American sector and the surrounding ocean areas, which is absent in the GIM difference TEC map. For GITM, the maximum TEC increase in this region reaches 20 TECU (against a quiet-time background of ~35 TECU); for TIE-GCM, the maximum TEC increase is less yet still around 10 TECU (against a quiet-time background of ~35 TECU). This TEC enhancement in the models is not temporary but persists for almost the entire storm period, whenever the region is experiencing a local daytime. For GITM, such enhancement has a larger longitudinal span than for TIE-GCM, as indicated by the narrow red band in panel (c) that covers more than 240 degrees in longitude. The similarity between GITM and TIE-GCM simulation results over the south American sector is particularly interesting given the many differences between the two models.

2.4 Modeling Experiments

To analyze the cause of the overestimation of the TEC response generated by both GITM and TIE-GCM, we perform experiments with both models. Since a forecastable-mode simulation is only driven by solar wind conditions and daily and 81-day averaged F10.7 indices, and recalling that the daily F10.7 index rose rapidly during the storm, we design the following three modeling experiments to evaluate the contribution of individual drivers to the overestimation of the TEC response:

- Test 1: simulation driven by a quiet solar wind and the actual F10.7 index

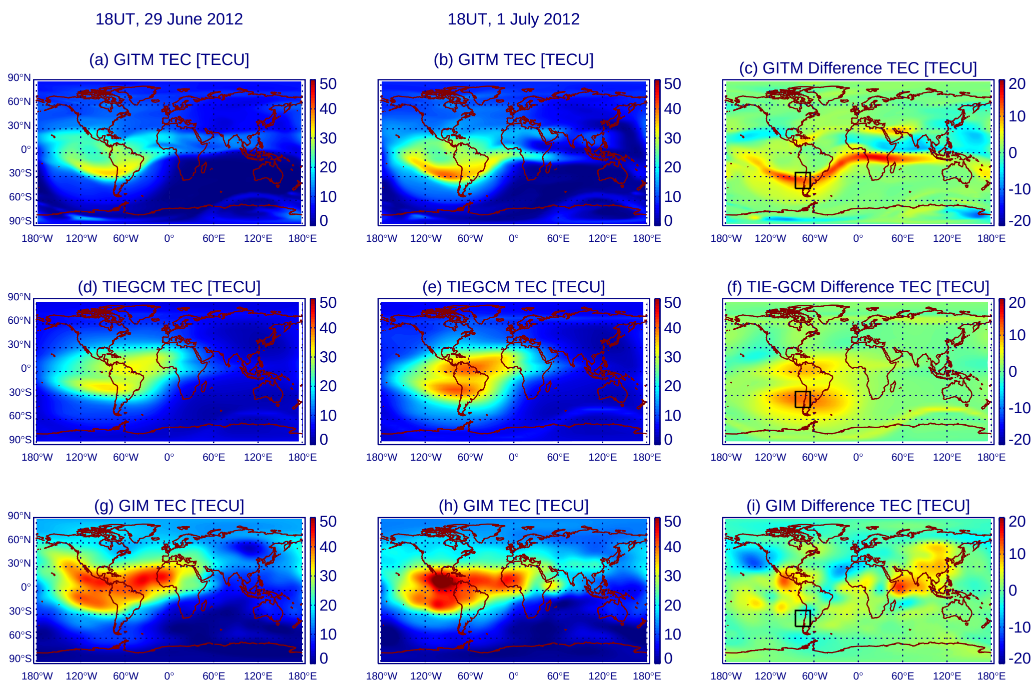

239 **Figure 4.** TEC maps from forecastable-mode GITM simulation (top row), forecastable-mode TIE-GCM simulation (middle row), GIM based on GPS-derived TEC data (bottom row). The quiet-time TEC map at 18UT on June 29, the storm-time TEC map at 18UT on July 1, and the difference TEC map at 18UT by subtracting the quiet-time TEC map at 18UT on June 29 from the storm-time TEC map at 18UT on July 1 are displayed in the left, middle, and right column, respectively. The black rectangle in panels (c), (f), (i) marks the region of interest, 85°W - 65°W and 45°S - 25°S.

- Test 2: simulation driven by a quiet F10.7 index and the actual solar wind conditions
- Test 3: simulation driven by a quiet solar wind and a quiet F10.7 index

Figure 1 shows the actual solar wind conditions in black and the synthesized quiet solar wind conditions in blue. The quiet solar wind is generated by mirroring the solar wind before the storm, starting at 12 UT on June 29, so the blue lines represent a backward propagating solar wind between 0 UT on June 26 and 12 UT on June 29. Synthesizing the solar wind input in this way not only retains the small oscillations from the actual solar wind parameters, but also avoids any discontinuities at the transition between the actual solar wind and the artificial quiet solar wind. Comparing the quiet solar wind to the actual solar wind between June 29 and July 2, the quiet solar wind no longer contains the CIR and the high-speed stream conditions that trigger the storm.

The F10.7 index is displayed in Figure 2. The synthesized quiet daily F10.7 index, represented by the green triangles, remains unchanged after June 29. The quiet 81-day center-averaged F10.7 index is calculated based on the quiet daily F10.7 index. By keeping the daily F10.7 index the same level during the storm days, the solar irradiance in the simulations remains the same as well.

All experiments are performed the same way as the original forecastable-mode runs for the same time interval. According to the design of the experiments, Test 1 would yield the ionospheric response to the increasing F10.7 index, Test 2 would produce the ionospheric response to the CIR and high-speed solar wind stream, and Test 3 would provide a baseline quiet ionosphere condition. Comparisons among the original run, Test 1, Test 2 and Test 3 would reveal the individual impact of the two drivers, the solar wind and F10.7 index, to the overestimation of the TEC response, for both GITM and TIE-GCM.

3 Results

We look into details of the modeling experiment results including the temporal and spatial variations of the TEC, the low-latitude electric field, the vertical ion drift, the solar irradiance spectrum, and the ion production rate via photoionization.

We select a small local geographic region 85°W - 65°W and 25°S - 45°S, maked as the green rectangle in Figure 3 and the black rectangle in Figure 4(c), (f), (i), where both

GITM and TIE-GCM forecastable-mode simulations show an overestimated TEC response. In addition, this is a region where the TEC from GIM is expected to be very accurate, since the data from multiple GPS ground receivers in the region were collected and used when GIM computes the TEC. We then calculate the mean TEC within this local region and visualize its hourly variation from the quiet day June 29 to the storm day July 2 in Figure 5. For each panel from top to bottom, the black line represents the hourly mean TEC on the quiet day June 29 from GITM, TIE-GCM, and GIM, respectively, repeated identically for every day. The red line in panel (a) represents the hourly mean TEC from the original forecastable-mode GITM run, and the other colored lines represent the hourly mean TECs from GITM tests. Panel (b) follows the same color code but for TIE-GCM. Panel (c) displays the corresponding GIM TEC data for comparison. The gray-shaded areas represent local night time from 6PM to 6AM. Comparing to the GIM data, the GITM and TIE-GCM original runs (red lines) generate much larger TEC increases relative to the quiet day during local daytime on June 30, July 1, and July 2. The overestimated TEC response is especially outstanding on July 2.

By driving the models with the quiet solar wind (Test 1, blue lines) or the quiet F10.7 (Test 2, green lines), the storm-time TEC reduces to some extent for both GITM and TIE-GCM comparing to the original run (red lines). With both quiet solar wind and quiet F10.7 (Test 3, yellow lines), the GITM and TIE-GCM simulated TEC remains very close to the quiet-day level, as expected. Depending on the day of the storm and the model, the consequences of quiet solar wind and quiet F10.7 vary. For GITM, Test 1 and Test 2 produce TECs of comparable magnitudes, which fall between the TECs from the original run and from Test 3. Two exceptions are: 1) during the daytime of July 1, the TEC from Test 1 has a similar magnitude as the TEC from the original run, while the TEC from Test 2 is much smaller and close to the quiet-time TEC. This indicates that for this time period, the disturbed and increasing F10.7 plays a major role in generating the TEC enhancement seen in the original GITM run. 2) during the local nights of July 1 and July 2, the TEC from Test 2 closely follows the TEC from the original run, which is much higher than the quiet-time TEC and TECs from Test 1 and Test 3. This could be explained by the absence of solar irradiance during local nighttime, so that the solar wind remains the only external contributor to the ionospheric TEC changes in the GITM simulations. For TIE-GCM, the TEC from Test 1 is almost always lower than the TEC from Test 2, while the TECs from both tests fall between the TEC from the original run and the TEC from

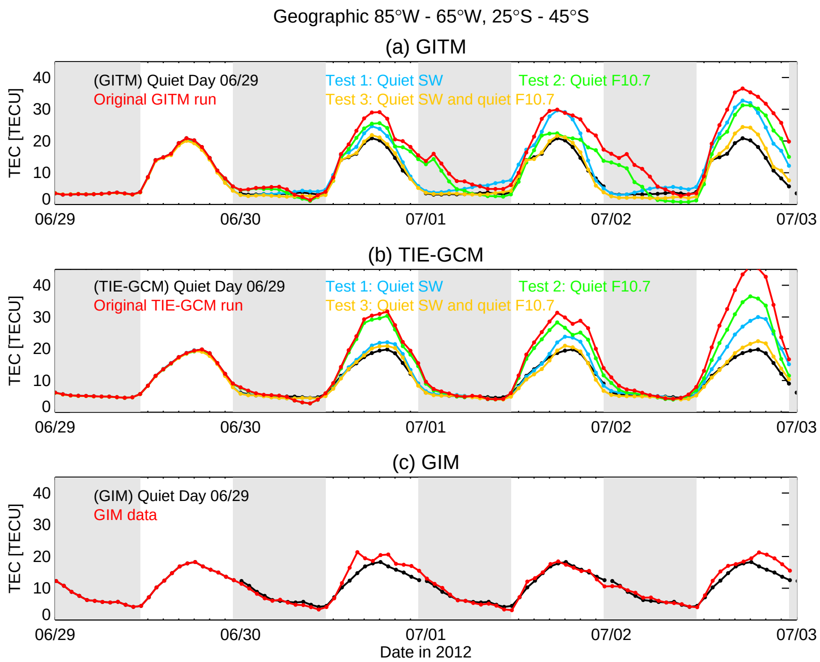

Figure 5. Timeseries of the mean TEC within the geographic region 85°W - 65°W, 25°S - 45°S from GITM (panel (a)), TIE-GCM (panel (b)) and GIM (panel (c)). The corresponding TEC on the quiet day June 29 is represented by the repeated black lines for every day. The gray-shaded areas represent the local time from 6PM to 6AM.

Test 3 or the quiet day. However, during the daytime of June 30, the TEC from Test 2 is very similar to the TEC from the original run, and the TEC from Test 1 is very similar to the TEC from the quiet day. This indicates that the disturbed solar wind dominates the TIE-GCM-simulated ionospheric TEC responses during the time interval.

Alternatively, for the different model runs and for GIM, we extract the TEC at the center longitude of the local region, 75°W for all latitudes and for every hour and subtract the quiet-day TEC of the corresponding model run or GIM from it. The resulting time-latitude contour plots are shown in Figure 6 for GIM and GITM, and in Figure 7 for GIM and TIE-GCM. Panel (a) in both Figures is the GIM difference TEC, which shows some TEC changes during the storm days from June 30 to July 2. The most prominent TEC changes are the enhancement in the northern hemispheric low-latitudinal region during the first few hours of July 1, corresponding to local night time, and the enhancement in the northern and southern low-latitudinal regions near the end of July 2, corresponding to the local late afternoon and evening. The maximum TEC enhancement does not exceed 15 TECU. On the contrary, GITM and TIE-GCM forecastable-mode runs (panel (b) in both Figures) clearly show strong TEC responses at southern hemispheric middle-low latitudinal region during the local day times of all storm days. In addition, the local nighttime TEC enhancement on July 1 from GIM is not captured by either model. Comparing to panel (e) representing modeling experiment Test 3, for which the TECs from both GITM and TIE-GCM show the minimal response, panels (c) and (d) reveal the impacts of the F10.7 driving and solar wind driving respectively. Test 1 shown in panel (c) of Figures 6 and 7 is driven by the quiet solar wind, and thus the TEC changes are mostly due to the elevated F10.7 index. Test 2 shown in panel (d) of both Figures is driven by the quiet F10.7 index, and thus the TEC changes are caused by the disturbed solar wind conditions only. Examining the TEC variations shown in panels (c), (d) and (e) of both Figures, the contributions from the disturbed solar wind and disturbed F10.7 in driving the southern hemispheric middle-low latitudinal TEC enhancement in the original runs are clear: 1) During the daytime, the disturbed solar wind has a much larger contribution than the disturbed F10.7 for the first day of the storm, June 30, for both GITM and TIE-GCM. For TIE-GCM, the contribution of the solar wind remains larger than, or at least comparable to, the contribution of the F10.7 during the daytime of July 1 and July 2. For GITM, the contribution of the solar wind becomes less than the contribution of the F10.7 during 14UT and 20UT (local 9AM to 3PM) on July 1, and the contributions are comparable during the daytime of July 2. 2) During the nighttime, the TEC responses are mainly controlled by the solar wind driving on all storm days. This holds true for both GITM and TIE-GCM forecastable-mode runs.

Comparisons between the simulated TECs and the GIM data at 75°W are shown in Figure 8 for three particular epochs: 18 UT on June 30, July 1, and July 2, that show the local daytime behavior (1PM local time). Panels (a), (c), and (e) shows the comparison between the GITM simulation results and the GIM data, and panels (b), (d), and (f) shows the TIE-GCM simulation results and the GIM data. In each panel, the dashed lines represent the latitudinal TEC distribution at 18UT on the quiet day June 29, while the solid lines represent the TEC at 18UT on the corresponding storm day. Both the quiet-time GITM solution and TIE-GCM solution deviate from the quiet-time GIM TEC. The discrepancy is more severe for GITM than for TIE-GCM. Comparing to GIM, both GITM

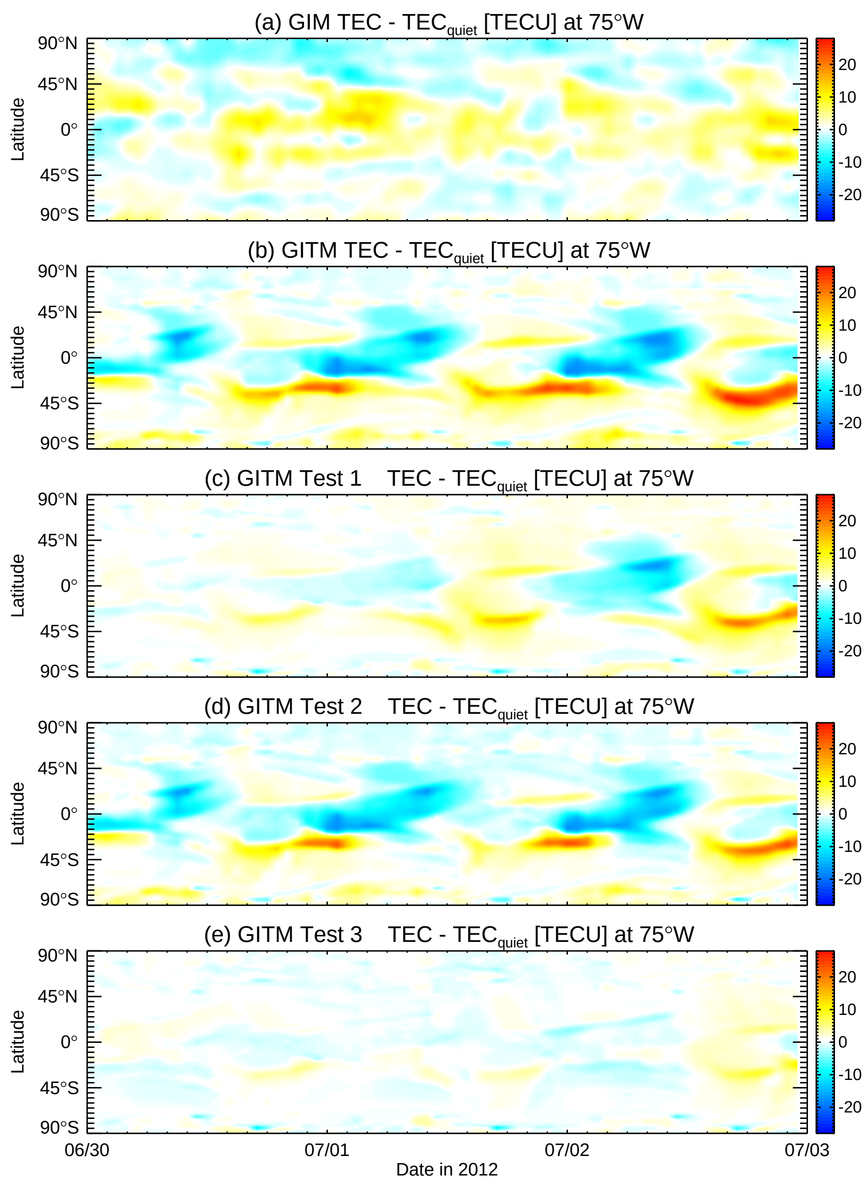

356 **Figure 6.** The difference TEC at 75°W from GIM (panel (a)), the original forecastable-mode GITM simu-
357 lation (panel (b)), Test 1 (panel (c)), Test 2 (panel (d)), and Test 3 (panel (e)). The difference TEC is taken by
358 subtracting the TEC on June 29 from the TEC on each day from June 30 to July 2.

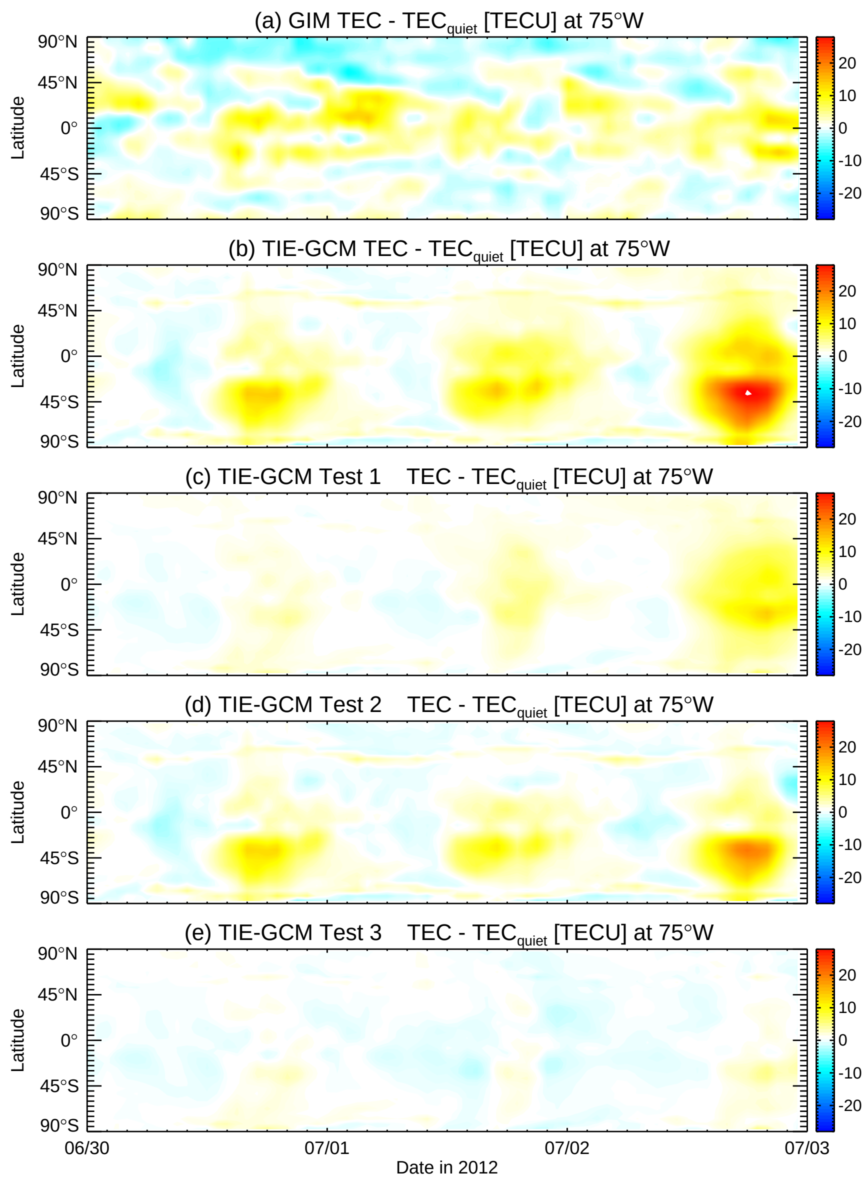

359 **Figure 7.** The same as Figure 6 but panels (b) through (e) are from TIE-GCM simulations.

and TIE-GCM underestimate the amplitude of the quiet-time TEC, which is partially due to the limited altitude range of GITM and TIE-GCM. In addition, the GIM quiet-time TEC has a larger peak in the northern hemisphere than in the southern hemisphere, while the GITM quiet-time TEC has a strong north-south asymmetry that peaks in the southern hemisphere. The TIE-GCM quiet-time TEC exhibits a weak north-south asymmetry, yet still peaks in the southern hemisphere. The difference in the north-south asymmetry of the TEC peaks, i.e., the equatorial ionospheric anomaly (EIA) crests, implies different quiet-time meridional neutral winds in the models and in reality (see Section 4).

Despite the difference in the quiet-time TEC between the simulations and data, we are more interested in the storm-time TEC response relative to the corresponding quiet-time TEC distribution for individual models and data. For GIM, the storm-time latitudinal TEC (black solid line) distribution shows increased TECs at the EIA crests at all three epochs, indicating a strengthened EIA during the storm. Among the three epochs, the most significant storm-time response is the TEC at the northern EIA crest (between 0° and 20°N) on June 30, which has an increase of around 10 TECU above the quiet-time level. Note that for GIM, the latitudinal locations of the storm-time EIA crests do not vary much from the quiet-time values, at least for the three epochs shown. Examining storm-time TECs from the original forecastable-mode GITM and TIE-GCM runs (red solid lines), both models produce an enhanced EIA during the storm. For GITM, the enhanced EIA is primarily characterized by the southward expansion of the southern EIA crest at all three epochs. The TEC at the southern EIA crest increases by 5 TECU at most, while the TEC at the northern EIA crest even decreases a little from the quiet-time value. For TIE-GCM, the enhanced EIA is characterized by both a significant increase of TECs at the EIA crests and a southward expansion of the EIA. The southward expansion of the EIA is not found in GIM. Moreover, both GITM and TIE-GCM do not capture the enhanced northern EIA crest in GIM on June 30.

Results from the three modeling experiments are also shown in Figure 8. First of all, the TEC from Test 3 (yellow line) is very similar to the quiet-time TEC for all three time epochs and for both GITM and TIE-GCM, as expected. Second, for GITM, the TEC from Test 2 (green line, left column) closely tracks the TEC from the quiet day at all latitudes at 18UT on June 30 and July 1, revealing the importance of the F10.7 driving in the determining the GITM-simulated EIA morphology. Third, for TIE-GCM, the TEC from Test 1 (blue line, right column) is almost always closer to the quiet-day TEC comparing to the

TEC from Test 2 (green line, right column), indicating that the solar wind driving is more important than the F10.7 driving in forming the EIA in TIE-GCM. However, an exception is at 18UT on July 2 (panel (f)), when the TEC from Test 2, instead of the TEC from Test 1, is closer to the quiet-time TEC for latitudes between 30°S and 90°N. This implies that the F10.7 driving takes over in dominating the TIE-GCM-simulated TEC response, which is not surprising given the highest increase of the daily F10.7 from July 1 to July 2 among all days.

The differences between the simulated storm-time and quiet-time EIAs suggest a difference in the low-latitude zonal electric field at storm and quiet times. Our region of interest is near the Jicamarca Unattended Long Term Investigations of the Ionosphere and Atmosphere (JULIA) radar location (77°W12°S), which can provide vertical ion drift data at 150 km altitude (http://jro-db.igp.gob.pe/madrigal/). Since the vertical ion drift is essentially the E×B drift, the variation in the vertical ion drift is almost entirely due to the change in the electric field E in the zonal direction. Therefore, by comparing the vertical ion drifts from the simulations and from the radar measurements, we could possibly assess the accuracy of the modeled low-latitude zonal electric field. Due to the availability of the JULIA ion drift data, we can only look at 9 AM (14 UT) to 17 PM (22 UT) on two storm days, June 30 and July 1. The results are shown in Figure 9. JULIA data is represented by the black asterisks, with vertical bars indicating measurement errors. For GITM and TIE-GCM, only the vertical ion drifts from the original run (red line) and Test 1 (blue line) are shown, because we find that the vertical ion drift from Test 2 (quiet F10.7) is almost identical to the original run, while the vertical ion drift from Test 3 (quiet solar wind and F10.7) is almost identical to the one from Test 1, for both models. In this case, the disturbed solar wind condition dominates over the disturbed F10.7 in influencing the low-latitude zonal electric field for both GITM and TIE-GCM. Figure 9 indicates that the original GITM and TIE-GCM runs overestimate vertical ion drifts in the morning of June 30 at Jicamarca, and the quiet solar wind driving helps reduce the vertical ion drifts to better match the JULIA data 9 AM to 11 AM, especially for GITM. The overestimation of the vertical ion drift is not seen in the morning of July 1, instead the original run produces similar drift velocities as Test 1 during the morning hours of July 1 for both GITM and TIE-GCM. Comparing drift velocity from the original GITM run on June 30 to the drift velocity from the same run on July 1, the latter is closer to the JULIA data for almost the entire time interval from 10 AM to 4 PM, indicating that the low-latitude zonal

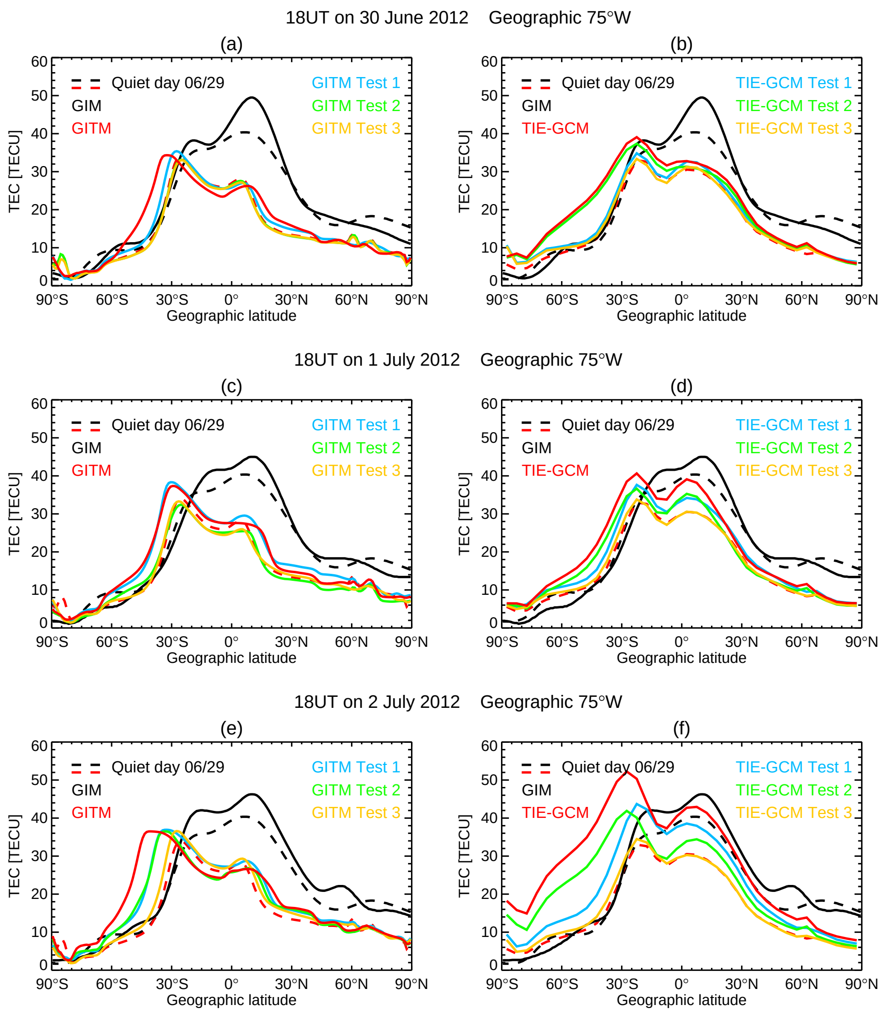

409 **Figure 8.** The TECs on the latitudinal cut at 75°W and at 18 UT on 30 June 2012 (top row), 1 July 2012
410 (middle row), and 2 July 2012 (bottom row) from GIM and GITM (left column), as well as from GIM and
411 TIE-GCM (right column).

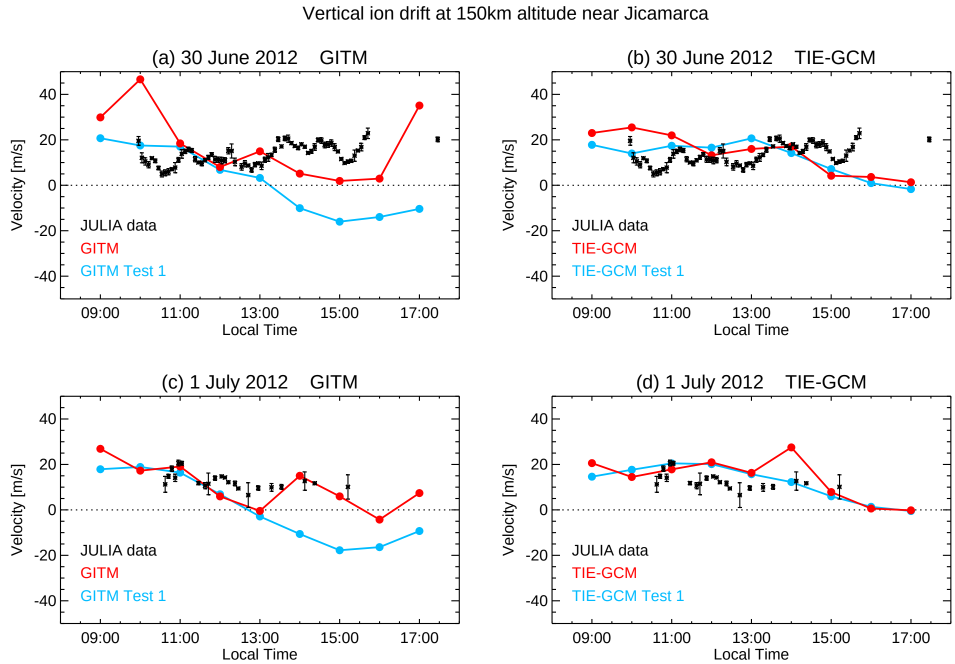

Figure 9. Comparisons of measured and simulated vertical ion drifts at 150 km altitude at Jicamarca on June 30 (upper panels) and July 1 (lower panels). The local time range from 9 AM to 17 PM corresponds to 14 UT to 22 UT on each day. The measurements are from the JULIA data, marked as black asterisks with vertical error bars.

electric field is more accurately reproduced by the GITM original run on July 1 than June 30. A similar conclusion can be drawn for TIE-GCM, yet the improvement from June 30 to July 1 is only during 10-11AM and insignificant. In addition, TIE-GCM seems to produce better matches with the JULIA data than GITM for most of the time on both days, which will be addressed in Section 4.

To evaluate the impact of F10.7 in more detail, we examine the photoionization rate of O from the GITM simulations, displayed in Figure 10. The photoionization of O is controlled by the incoming solar irradiance, and provides the major ion source at the F layer. The four panels in Figure 10 show the photoionization rate in the latitude-altitude plane at 75° and at 18 UT on July 1 (storm day) from the original run, Test 1, Test 2, and Test 3, respectively. A comparison among the four panels reveals that the quiet F10.7 condition reduces the photoionization of O significantly, indicating that the disturbed F10.7

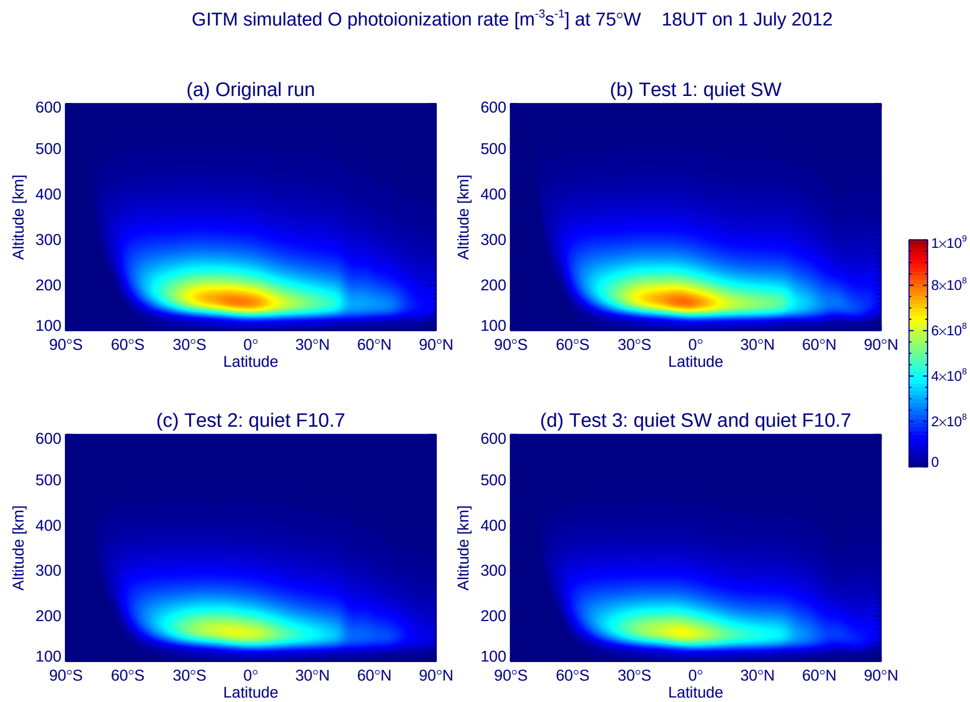

Figure 10. GITM simulated O photoionization rate at the longitudinal cut 75°W and 18UT on July 1 from the original run (panel (a)), Test 1 (panel (b)), Test 2 (panel (c)), and Test 3 (panel (d)).

contributes to the TEC enhancement by intensifying the photoionization of O with increased solar irradiance.

In the forecastable-mode GITM and TIE-GCM simulations, the solar irradiance spectrum is determined similarly via several empirical models based on the daily and 81-day center-averaged F10.7 indices. The solar irradiance between 0.5 nm and 5 nm and between 105 nm and 175 nm comes from the Hinteregger model [*Hinteregger*, 1981] and Woods and Rottman model [*Woods and Rottman*, 2002], respectively. Most importantly, the solar irradiance between wavelengths 5 nm and 105 nm, the extreme ultraviolet (EUV) part of the spectrum, is specified by empirical model EUVAC for TIE-GCM, and by the average of the solar irradiance from EUVAC and Tobiska91 models for GITM. In Figure 11, we compare the empirically specified solar irradiance spectrum to the actual solar spectrum measured by the Thermosphere Ionosphere Mesosphere Energetics and Dynamics (TIMED)/Solar EUV Experiment (SEE) [*Woods et al.*, 2005] from 0.5 nm to 115 nm and by Solar Radiation and Climate Experiment (SORCE) [*Rottman*, 2005] above 115 nm for two days. From June 29 to July 2, the daily F10.7 keeps increasing, and the resulting GITM-modeled solar irradiance (black and red dashed lines) also increases over these days. Significant solar irradiance enhancements are seen at around 120 nm and between 50 nm and 105 nm in the modeled solar irradiance spectrum. However, these enhancements are absent in the measured spectra, despite the increasing daily F10.7 index. The EUV solar irradiance from the EUVAC alone are shown as the blue and yellow dashed lines in panel (b). Comparing to the EUV solar irradiance from the average of the EUVAC and Tobiska91, the EUVAC better matches the measurement, and the enhancement of irradiance from June 29 to July 2 is smaller, though still present. Note that the EUVAC spectra shown in the figure is from the EUVAC model used by GITM, which is based on the F74113 solar reference spectrum. The EUVAC model used by TIE-GCM is based on SC21REFW reference spectrum [*Solomon and Qian*, 2005]. Despite the differences between these reference spectra, the dependence on F10.7 remains the same. Therefore, we anticipate that the EUV solar irradiance in TIE-GCM has a similar enhancement from June 29 to July 2 as shown by the blue and yellow dashed lines. In summary, the solar irradiance enhancement in GITM and TIE-GCM during the June 2012 event is overestimated by the empirical models, which induces the overestimation of the O photoionization rate and thus the daytime TEC in the region of interest.

4 Discussion

The modeling experiments indicate that both the disturbed solar wind and the enhanced solar irradiance lead to the southern hemispheric middle-low latitudinal overestimation of the storm-time TEC response produced by forecastable-mode simulations of GITM and TIE-GCM. In particular, the contribution from the solar wind dominates over the contribution from the solar irradiance on the first day of the storm, while the contribution from the solar irradiance becomes comparable to or even larger than the contribution from the solar wind on later days of the storm. This implies that the simulated daytime TEC enhancement over the middle-low latitude region is initially due to the CIR passage and then the apparent increase in modeled solar irradiance based on the F10.7 proxy, both resulting in an overestimated TEC response compared to the GIM data.

The solar wind condition, interplanetary magnetic field included, affects the ionospheric solution via the high-latitude electric field, computed by the Weimer empirical model in both GITM and TIE-GCM. This high-latitude electric field also determines the

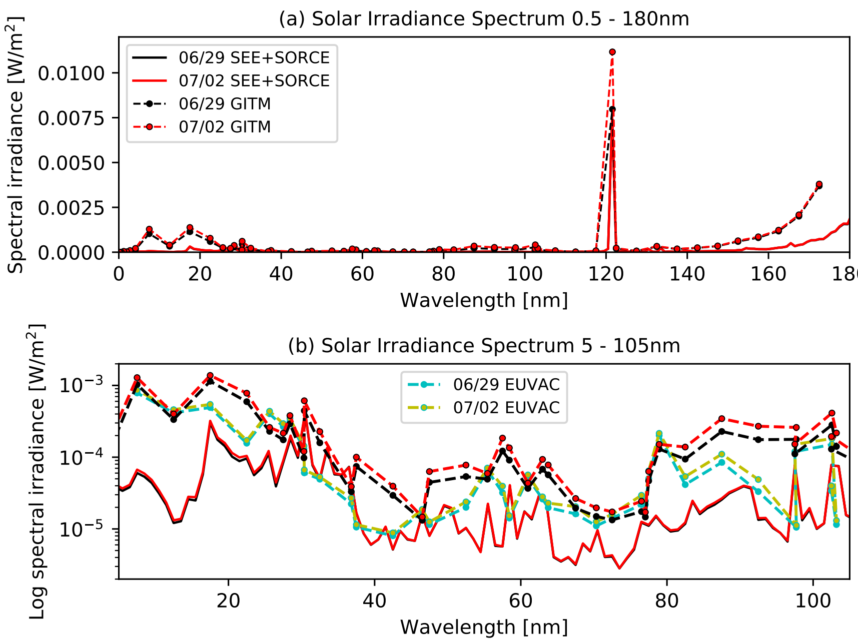

Figure 11. Comparisons of measured (solid lines) and empirically modeled (dots connected with black and red dashed lines) solar irradiance spectra between 0.5 and 180 nm (upper panel) and between 5 and 105 nm (lower panel) for two days during the 2012 event: June 29 and July 2. The empirically modeled spectra are from the models used by GITM. The EUV spectra from the EUVAC model alone is shown as dots connected with blue and yellow dashed lines in panel (b).

behavior of the low-latitude electric field to a large extent, based on the comparison among vertical ion drifts from the modeling experiments (referring back to the earlier discussion on Figure 9). Interestingly, the low-latitude electric fields from GITM and TIE-GCM are different, despite the almost identical low-latitude electrodynamic solvers in the two models and the identical drivers for the two models. As shown in Figure 9, TIE-GCM has a better comparison with the JULIA vertical ion drift data than GITM on June 30, the first day of the storm. Moreover, GITM Test 1 yields unrealistic downward ion drift in the local afternoons, deviating from the JULIA data and the TIE-GCM result significantly. The difference between GITM- and TIE-GCM-modeled vertical ion drift could be caused by different atmospheric tide specifications at the lower boundary of the two models: GITM uses the MSIS tide and TIE-GCM applies the more advanced Global Scale Wave Model. A more realistic tide representation at the lower boundary could potentially improve the electrodynamics [*Vichare et al.*, 2012]. Despite the better represented tide, TIE-GCM still overestimates the zonal electric field near Jicamarca during the local morning time on June 30. This discrepancy could be caused by 1) the inaccurate high-latitude electric field produced by the Weimer model [*Weimer*, 2005a; *Kihn et al.*, 2006; *Gordeev et al.*, 2015; *Yu et al.*, 2017]; 2) the lack of a ring current model to provide self-consistent Region 2 field-aligned currents, which could possibly lead to a more accurate low-latitude electric field [*Richmond et al.*, 2003; *Wang et al.*, 2008]. Moreover, *Zhu et al.* [2017] shows that a better low and middle latitude electrodynamic solver for GITM would improve the modeled zonal electric field and thus the EIA morphology. On a side note, discrepancies between simulated EIAs from various models, GITM and TIE-GCM included, have been shown by *Fang et al.* [2014] for a geomagnetically quiet day and by *Shim et al.* [2018] for a geomagnetic storm. Both studies attribute the cause of the discrepancies to the different lower boundary forcings and electric fields in different models.

The solar irradiance, especially the EUV irradiance, is the primary energy source for the upper atmosphere. The accuracy of the solar EUV irradiance input to GITM and TIE-GCM directly affects the accuracy of the modeled electron production via the O photoionization. For the solar EUV irradiance specification, both GITM and TIE-GCM rely on the EUVAC model, which is an empirical model based on the daily F10.7 index and its 81-day average [*Richards et al.*, 1994]. In addition to the EUVAC model, GITM also applies the Tobiska91 model, and the resulting EUV spectrum is calculated as the mean of the EUVAC and the Tobiska91 spectra. The underlying assumption of the EUVAC model and the Tobiska91 model is that the EUV irradiance scales linearly with the mean of the F10.7 index and its 81-day average. Since the 81-day average F10.7 does not vary much from June 29 to July 2 (Figure 2), the simulated solar irradiance is mostly controlled by the F10.7 index that rises quickly during this time period, resulting in the overestimated irradiance increase (Figure 11). The combined EUVAC and Tobiska91 spectrum is more sensitive to the daily F10.7 increase than the EUVAC spectrum alone (panel (b) of Figure 11). This explains earlier results that the F10.7 driving controls the GITM-simulated TEC response than the TIE-GCM-simulated TEC response. Such differences in TEC responses from GITM and TIE-GCM could also lead to different low-latitude electric fields in GITM and TIE-GCM via ionospheric conductivities.

The overestimation of the solar irradiance increase from empirical models could be due to either the inaccuracy of the F10.7 index itself or the limitation of F10.7 as a proxy for the EUV irradiance. For the former, the uncertainties of the F10.7 measurement and determination have been discussed in *Tapping and Charrois* [1994]; *Tapping* [2013] and supported by *Schonfeld et al.* [2015] thus not repeated here. For the latter, a number of studies [*Hedin*, 1984; *Donnelly et al.*, 1986; *Lean*, 1988; *Tobiska*, 1996; *Floyd et al.*, 2005; *Wintoft*, 2011; *Chen et al.*, 2011; *Huang et al.*, 2015] have shown that the correlation between the F10.7 index and the EUV irradiance varies over different time scales and with solar activity levels, therefore the variation in F10.7 cannot fully represent the variation in the EUV irradiance. Alternatively, several studies [*Viereck et al.*, 2001; *Floyd et al.*, 2005; *Wintoft*, 2011; *Chen et al.*, 2012] have shown that the Mg II core-to-wing ratio reproduces the short-term EUV irradiance variation better than F10.7 for emission wavelengths between 25 nm and 35 nm.

To further evaluate the impact of the solar irradiance on the modeling results, we perform an additional experiment with GITM, driven by the disturbed solar wind and the solar irradiance at wavelengths between 0.1 nm and 190 nm provided by the Flare Irradiance Spectral Model (FISM) that includes solar flare contributions [*Chamberlin et al.*, 2008] for the time interval of June 29 - July 2. Comparing to the EUVAC, Tobiska91, Hinteregger, and Woods and Rottman models that are based on a reference spectrum and daily values of F10.7, FISM is constructed from actual solar irradiance measurements by multiple satellites and has a higher spectral resolution (1 nm) and a much finer temporal resolution (one minute). The FISM-provided solar irradiance has less increase over the days of interest (not shown) and thus is more realistic than the solar irradiance used in the original GITM run. Figure 12 displays the GITM-simulated mean TEC within the local region of interest as for Figure 5. The result from the new experiment, noted by Test 4, is represented by the magenta line, and the result from the original forecastable-mode run is represented by the red line. Results from Test 1 and Test 2 are also displayed for comparison. The TEC from Test 4 is very similar to the TEC from the original run until the middle of July 1, when the former starts to deviate from the latter. From the middle of July 1 to the end of July 2, Test 4 produces significantly less TEC than the original run does. At the TEC diurnal peak of July 2, the TEC reduction caused by changing the solar irradiance specification from F10.7-based models to FISM (the original run versus Test 4) is comparable to the TEC reduction caused by replacing the disturbed solar wind with the quiet solar wind (the original run versus Test 1) or replacing the disturbed F10.7 with the quiet F10.7 (the original run versus Test 2). Comparing to the original run, the FISM-driven Test 4 generates more realistic mean TEC within the region of interest on July 1 and July 2. However, Test 4 still overestimates the TEC response during the entire storm comparing to the GIM TEC shown in Figure 5, for which uncertainties in the GITM-modeled zonal electric field and the uncertainties in FISM for reproducing the actual solar irradiance could be significant factors. In summary, the new test result implies that the modeled TEC could be improved with a better solar irradiance specification.

For thermospheric-ionospheric forecasts with a lead time of a few days, one needs to provide forecasted solar wind conditions and solar irradiance to drive the physics-based thermospheric-ionospheric models. Our present study is indicative of inaccuracies can occur even if such inputs are forecasted perfectly. Additional uncertainties in imperfectly forecasted drivers will likely lead to modeling results with less fidelity than the forecastable-mode modeling results presented here. Therefore, maintaining and improving the performance of the thermospheric-ionospheric models is critical. According to this case study, the modeled low-latitude zonal electric field is not sufficiently accurate to prevent large errors in the modeled low-latitude TEC near the EIA region. Problems with the solar EUV proxy can similarly produce relatively large errors in the EIA region during daytime. Any improvements have to be consistent with the concept of “forecast” and allow forecastable inputs. For instance, the setting of the FISM-driven GITM test is not applicable for actual forecasts, since FISM relies on measurements that are not available ahead of time. However, TIE-GCM driven by the solar irradiance calculated based on Mg II index [*Solomon et al.*, 2011] can offer an alternative “forecastable-mode” setting.

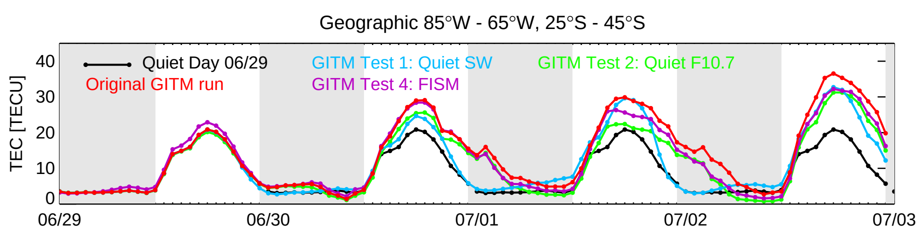

Figure 12. Timeseries of the mean TEC within the geographic region 85°W - 65°W, 25°S - 45°S from the forecastable-mode GITM run driven by the disturbed solar wind and F10.7, Test 1 driven by the quiet solar wind and actual F10.7, Test 2 driven by the disturbed solar wind and quiet F10.7, and Test 4 driven by the disturbed solar wind and FISM. The corresponding TEC on the quiet day June 29 is represented by the repeated black lines for every day.

In addition to the overestimated storm-time response by GITM and TIE-GCM, our results also reveal the inaccuracy of the models in capturing quiet-time ionospheric conditions. Displayed in Figure 8, the inter-hemispheric asymmetry of the quiet-time EIA crests at 18 UT on June 29 is not well reproduced by GITM or TIE-GCM. The GIM TEC data suggest a northward neutral wind at the F-layer that causes the northern hemispheric EIA crest more enhanced than the southern hemispheric EIA crest. GITM produces an opposite asymmetry, suggesting a neutral wind blowing from northern hemisphere to the southern hemisphere at the F-layer (confirmed by looking at the GITM modeled neutral wind: about 20 m/s southward at the equator); TIE-GCM produces less asymmetry comparing to GITM, suggesting a weaker meridional wind at the F-layer (confirmed by looking at the TIE-GCM modeled neutral wind: about 5 m/s southward at the equator). During quiet time, the modeled meridional wind in the ionosphere and thermosphere is largely controlled by the tidal forcing at the lower boundary of the models, implying the importance of the tidal forcing in determine the inter-hemispheric asymmetry of the quiet-time EIA. This topic requires further attention, but it is beyond the scope of the current paper. As a final note, the forecastable-mode simulations cannot take full advantage of the state-of-the-art modeling approaches including inputs based on past direct observations, and thus they almost certainly perform worse than the simulations set up under the best practice.

5 Conclusion

To explore the forecast capability of the current first-principles thermospheric-ionospheric models, we have defined "forecastable-mode" model runs that are driven solely by solar wind conditions and the solar EUV irradiance proxy F10.7. These simulations are considered "forecastable" because there are current efforts to produce forecasts of these driver quantities with few-day lead times. Such forecasted drivers could be used to forecast ionospheric conditions in the type of simulations used here. We investigate modeling errors that can occur using the measured drivers as input, i.e. if the forecasted drivers were as accurate as those observed. We do not investigate additional forecast errors that might arise from errors in the drivers.

We have performed forecastable-mode simulations with GITM and TIE-GCM for the June 2012 high-speed-stream weak geomagnetic storm. The simulation results are compared to the GIM, which is based on GPS TEC observations. We find general agreement between the models and the GIM in terms of the storm-time TEC response, i.e., the difference between storm-time and quiet-time TECs. However, we also find overestimation of the storm-time TEC response in the middle-low latitude region of the southern American sector and surrounding areas from both models compared to the GIM. We focus on a local region where both GITM and TIE-GCM overestimate the TEC response to the storm during similar time periods and where the GPS ground receivers are ample. These overestimations well exceed the expected error of the GIM in the local region, where the nearby GPS ground receivers help maintain the accuracy of the GIM. As the forecastable-mode modeling is driven by the solar wind condition and the F10.7 index only, we design and perform three modeling experiments with each model to determine how the drivers might contribute to the overestimation of the TEC response. For each model, the three tests are identical to the original forecastable-mode run except with different drivers: one test driven by a quiet solar wind and the actual F10.7, one test driven by a quiet F10.7 index and the actual solar wind, and one test driven by a quiet solar wind and a quiet F10.7 index. The comparisons among the TECs from the three tests and from the original run reveal that the models reasonably produce TEC increases due to increases in the daily F10.7 index and due to the CIR/HSS in the solar wind, but the TEC increases did not actually occur according to the GIM data.

On the first day of the storm, the overly estimated TEC response in the middle-low latitude region is due to the solar wind driving that produces overestimated daytime EIA response in both GITM and TIE-GCM forecastable-mode simulations. By comparing the modeled vertical ion drifts to the observed ones, we show that the models, especially GITM, overestimate the low-latitude zonal electric field, in response to the actual solar wind conditions occurring during the CIR/HSS. Under the constraint of the forecastable-mode setting, forecasting improvements may be realized with 1) changes in the tidal forcing at the lower boundary of the models, 2) changes in the low and middle latitude electrodynamic solver, and 3) an improved high-latitude empirical electric field model.

The mismatch between the solar irradiance based on F10.7 index and the actual solar irradiance contributes to the overestimation after the first day of the storm. For GITM, the contribution of the mismatch is even larger than the contribution of the solar wind on the second day of the storm. We find the F10.7-based solar irradiance proxy models used by GITM and TIE-GCM fail to represent the measured solar irradiance variations. The modeled solar irradiance increases much more than observed over the storm days. The rapidly increasing F10.7 index during the storm led to increased simulated solar EUV irradiance, in contrast to actual irradiance values that were nearly constant. The unrealistic intensification of the simulated solar irradiance results in a high atomic oxygen photoionization rate and thus an enhanced electron production in the models, which leads to the overestimation of the TEC response. Our additional modeling experiment driven by FISM reveals that a better solar irradiance model could improve the modeled TEC. Improvements to the existing proxy-based solar irradiance models will lead to improved forecast accuracy of the ionospheric TEC with the physics-based thermospheric-ionospheric models.

Acknowledgments

This work was done at the Jet Propulsion Laboratory, California Institute of Technology, under contract with NASA. The authors gratefully acknowledge Dr. Wenbin Wang and Dr. Tong Dang at UCAR for discussions on TIE-GCM, the TIE-GCM developers and the Commnunity Coordinated Modeling Center (CCMC) for performing the TIE-GCM runs. The GIM data is available at `https://sideshow.jpl.nasa.gov/pub/iono_daily/gim_for_research/jpli/2012/`. The GITM run outputs are available at `https://data.nasa.gov/Space-Science/Thermosphere-Ionosphere-Modeling-with-Forecastable/pv8a-zybu`. The TIE-GCM run outputs are available at the CCMC simulation results database (`https://ccmc.gsfc.nasa.gov/ungrouped/search_main.php`) with run numbers Xing_Meng_060517_IT_1 to Xing_Meng_060517_IT_4. The authors also thank Dr. Ed Thiemann at UC Boulder for discussions on FISM. The Jicamarca Radio Observatory is gratefully acknowledged for providing the JULIA vertical drift data (`http://jro-db.igp.gob.pe/madrigal/`). The TIMED/SEE and SORCE solar spectral irradiance data are obtained via LISIRD: `http://lasp.colorado.edu/lisird/data/timed_see_ssi_l3/` and `http://lasp.colorado.edu/lisird/data/sorce_ssi_l3/`. The authors also thank J. H. King, N. Papatashvilli at AdnetSystems, NASA GSFC and CDAWeb for providing the OMNI data (`http://cdaweb.gsfc.nasa.gov/istp_public/`). The GITM computing resources were provided by the NASA High-End Computing Program through the NASA Advanced Supercomputing Division at Ames Research Center.

References

Chamberlin, P. C., T. N. Woods, and F. G. Eparvier (2008), Flare irradiance spectral model (FISM): Flare component algorithms and results, *Space Weather*, *6*, S05,001.

Chartier, A. T., T. Matsuo, J. L. Anderson, N. Collions, T. J. Hoar, G. Lu, C. N. Mitchell, A. J. Coster, L. J. Paxton, and G. S. Bust (2016), Ionospheric data assimilation and forecasting during storms, *J. Geophys. Res.*, *121*, 764–778.

Chen, C. H., C. H. Lin, T. Matsuo, W. H. Chen, I. T. Lee, J. Y. Liu, J. T. Lin, and C. T. Hsu (2016), Ionospheric data assimilation with thermosphere-ionosphere-electrodynamics general circulation model and GPS-TEC during geomagnetic storm conditions, *J. Geophys. Res.*, *121*, 5708–5722.

Chen, Y., L. Liu, and W. Wan (2011), Does the F10.7 index correctly describe solar EUV flux during the deep solar minimum of 2007-2009?, *J. Geophys. Res.*, *116*, A04,304.

Chen, Y., L. Liu, and W. Wan (2012), The discrepancy in solar EUV-proxy correlations on solar cycle and solar rotation timescales and its manifestation in the ionosphere, *J. Geophys. Res.*, *117*, A03,313.

Donnelly, R. F., H. E. Hinteregger, and D. F. Heath (1986), Temporal variations of solar EUV, UV, and 10,830-Å radiation, *J. Geophys. Res.*, *91*(A5), 5567–5578.

Drob, D. P., J. T. Emmert, G. Crowley, J. M. Picone, G. G. Shepherd, W. Skinner, P. Hays, R. J. Niciejewski, M. Larsen, C. Y. She, J. W. Meriwether, G. Hernandez, M. J. Jarvis, D. P. Sipler, C. A. Tepley, M. S. O'Brien, J. R. Bowman, Q. Wu, Y. Murayama, S. Kawamura, I. M. Reid, and R. A. Vincent (2008), An empirical model of the earth's horizontal wind fields: HWM07, *J. Geophys. Res.*, *113*(A12304), doi: 10.1029/2008JA013668.

Emery, B. A., V. Coumans, D. S. Evans, G. A. Germany, M. S. Greer, E. Holeman, K. Kadinsky-Cade, F. J. Rich, and W. Xu (2008), Seasonal, Kp, solar wind, and solar flux variations in long-term single-pass satellite estimates of electron and ion auroral hemispheric power, *J. Geophys. Res.*, *113*, A06,311.

Fang, T., D. Anderson, T. Fuller-Rowell, R. Akmaev, M. Codrescu, G. Millward, J. Sojka, L. Scherliess, V. Eccles, J. Retterer, J. Huba, G. Joyce, A. Richmond, A. Maute, G. Crowley, A. Ridley, and G. Vichare (2014), Comparative studies of theoretical models in the equatorial ionosphere, in *Modeling the Ionosphere-Thermosphere System*, edited by J. Huba, R. Schunk, and G. Khazanov, pp. 133–144, John Wiley, doi: 10.1002/9781118704417.ch12.

Floyd, L., J. Newmark, J. Cook, L. Herring, and D. McMullin (2005), Solar EUV and UV spectral irradiances and solar indices, *J. Atmos. Solar-Terr. Phys.*, *67*, 3–15.

Gonzalez, W. D., J. A. Joselyn, Y. Kamide, H. W. Kroehl, G. Rostoker, B. T. Tsurutani, and V. M. Vasyliunas (1994), What is a geomagnetic storm?, *J. Geophys. Res.*, *99*(A4), 5771–5792.

Gordeev, E., V. Sergeev, I. Honkonen, M. Kuznetsova, L. Rastätter, M. Palmroth, P. Janhunen, G. Tóth, J. Lyon, and M. Wiltberger (2015), Assessing the performance of community-available global MHD models using key system parameters and empirical relationships, *Space Weather*, *13*, 868–884.

Hedin, A. (1991), Extension of the MSIS thermosphere model into the middle and lower atmosphere, *J. Geophys. Res.*, *96*, 1159, doi:10.1029/90JA02125.

Hedin, A. E. (1984), Correlations between thermospheric density and temperature, solar EUV flux, and 10.7-cm flux variations, *J. Geophys. Res.*, *89*(A11), 9828–9834.

Henney, C. J., R. A. Hock, A. K. Schooley, W. A. Toussaint, S. M. White, and C. N. Arge (2015), Forecasting solar extreme and far ultraviolet irradiance, *Space Weather*, *13*, 141–153.

Hernandez-Pajares, M., J. M. Juan, J. Sanz, R. Orus, A. Garcia-Rigo, J. Feltens, A. Komjathy, S. C. Schaer, and A. Krankowski (2009), The igs vtec maps: a reliable source of ionospheric information since 1998, *J Geod*, *83*, 263–275.

Hinteregger, H. E. (1981), Representations of solar euv fluxes for aeronomical applications, *Adv. Space Res.*, *1*, 39 – 52.

Ho, C., B. Wilson, A. Mannucci, U. Lindqwister, and D.N.Yuan (1997), A comparative study of ionospheric total electron content measurements using global ionospheric maps of gps, topex radar, and the bent model, *Radio Science*, *32*, 1499–1512.

Huang, J., Y. Hao, D. Zhang, and Z. Xiao (2015), Changes of solar extreme ultraviolet spectrum in solar cycle 24, *J. Geophys. Res.*, *121*, 6844–6854.

Huba, J. D., G. Joyce, and J. A. Fedder (2000), Sami2 is another model of the ionosphere (SAMI2): A new low-latitude ionosphere model, *J. Geophys. Res.*, *105*(A10), 23,035–23,053, doi:0.1029/2000JA000035.

Iijima, B. A., I. L. Harris, C. Ho, U. Lindgqwister, A. J. Mannucci, X. Pi, M. J. Reyes, L. C. Sparks, and B. D. Wilson (1999), Automated daily process for global ionospheric total electron content maps and satellite ocean altimeter ionospheric calibration based on global positioning system data, *J. Atmos. Solar-Terr. Phys.*, *61*, 1205–1218.

Jian, L. K., P. J. MacNeice, A. Taktakishvili, D. Odstrcil, B. Jackson, H.-S. Yu, P. Riley, I. V. Sokolov, and R. M. Evans (2015), Validation for solar wind prediction at earth: Comparison of coronal and heliospheric models installed at the CCMC, *Space Weather*, *13*, 316–338.

Keil, M. (2007), Numerical space weather prediction: Can meteorologists forecast the way ahead?, in *Space Weather: Research Towards Applications in Europe*, edited by J. Lilensten, pp. 115–124, Springer.

Kihn, E. A., M. Zhizhin, and Y. Kamide (2006), An analog forecast model for the high-latitude ionospheric potential based on assimilative mapping of ionospheric electrodynamics archives, *Space Weather*, *4*, S05,001, doi:10.1029/2005SW000199.

Lean, J. (1988), Solar EUV irradiances and indices, *Adv. Space Res.*, *8*(5-6).

Lu, G., M. E. Hagan, K. Hausler, E. Doornbos, S. Bruinsma, B. J. Anderson, and H. Korth (2015), Global ionospheric and thermospheric response to the 5 April 2010 geomagnetic storm: An integrated data-model investigation, *J. Geophys. Res.*, *119*, 10,358–10,375.

Mannucci, A. J., B. D. Wilson, D. N. Yuan, C. H. Ho, U. J. Lindqwister, and T. F. Runge (1998), A global mapping technique for gps-derived ionospheric total electron content measurements, *Radio Sci.*, *33*, 565–582.

Mannucci, A. J., O. P. Verkhoglyadova, B. T. Tsurutani, X. Meng, X. Pi, C. Wang, G. Rosen, E. Lynch, S. Sharma, A. Ridley, W. Manchester, B. van der Holst, E. Echer, and R. Hajra (2015), Medium-range thermosphere-ionosphere storm forecasts, *Space Weather*, *13*, 125–129, doi:1002/2014SW001125.

Mannucci, A. J., M. E. Hagan, A. Vourlidas, C. Y. Huang, O. P. Verkhoglyadova, and Y. Deng (2016), Scientific challenges in thermosphere-ionosphere forecasting - conclusions from the October 2014 NASA JPL community workshop, *J. Space Weather Space Clim.*, *6*, E01.

Matsuo, T., I.-T. Lee, and J. L. Anderson (2013), Thermospheric mass density specification using an ensemble kalman filter, *J. Geophys. Res.*, *118*(1339-1350).

Maute, A. (2017), Thermosphere-ionosphere-electrodynamics general circulation model for the ionospheric connection explorer: Tiegcm-icon, *Space Science Reviews*, *212*(523-551).

Meng, X., A. J. Mannucci, O. P. Verkhoglyadova, and B. T. Tsurutani (2016), On forecasting ionospheric total electron content responses to high-speed solar wind streams, *J.*

Space Weather Space Clim., *6*(A19), doi:10.1051/swsc/2016014.

Millward, G. H., R. J. Moffett, S. Quegan, and T. J. Fuller-Rowell (1996), A coupled thermosphere ionosphere plasmasphere model (CTIP), in *STEP Handbook on Ionospheric Models*, edited by R. W. Schunk, pp. 239–279, Utah State Univ., Logan.

Newell, P. T., T. Sotirelis, and S. Wing (2009), Diffuse, monoenergetic, and broadband aurora: The global precipitation budget, *J. Geophys. Res.*, *114*(A09207), doi:10.1029/2009JA014326.

Owens, M. J., H. E. Spence, S. McGregor, W. J. Hughes, J. M. Quinn, C. N. Arge, P. Riley, J. Linker, and D. Odstrcil (2008), Metrics for solar wind prediction models: Comparison of empirical, hybrid, and physics-based schemes with 8 years of L1 observations, *Space Weather*, *6*, S08,001.

Qian, L., S. C. Solomon, R. Roble, B.R.Bowman, and F.A.Marcos (2008), Thermospheric neutral density response to solar forcing, *Advances in Space Research*, *42*(5), 926 – 932, doi:https://doi.org/10.1016/j.asr.2007.10.019.

Qian, L., A. G. Burns, B. A. Emery, B. Foster, G. Lu, A. Maute, A. D. Richmond, R. G. Roble, S. C. Solomon, and W. Wang (2014), *The NCAR TIE-GCM*, chap. 7, pp. 73–83, American Geophysical Union (AGU), doi:10.1002/9781118704417.ch7.

Richards, P. G., J. A. Fennelly, and D. G. Torr (1994), EUVAC: A solar EUV flux model for aeronomic calculations, *J. Geophys. Res.*, *99*, 8981–8992.

Richmond, A. D., E. C. Ridley, and R. G. Roble (1992), A thermosphere/ionosphere general circulation model with coupled electrodynamics, *Geophys. Res. Lett.*, *19*, 369, doi:10.1029/92GL00401.

Richmond, A. D., C. Peymirat, and R. G. Roble (2003), Long-lasting disturbances in the equatorial ionospheric electric field simulated with a coupled magnetosphere-ionosphere-thermosphere model, *J. Geophys. Res.*, *108*, 1118, doi:10.1029/2002JA009758.

Ridley, A. J., Y. Deng, and G. Tóth (2006), The global ionosphere-thermosphere model, *J. Atmos. Solar-Terr. Phys.*, *68*, 839–864, doi:10.1016/j.jastp.2006.01.008.

Roble, R. G., and E. C. Ridley (1994), A thermosphere-ionosphere-mesosphere-electrodynamics general circulation model (TIME-GCM): equinox solar cycle minimum simulations (30-500 km), *Geophys. Res. Lett.*, *21*(417), doi:10.1029/93GL03391.

Rottman, G. (2005), The SORCE mission, *Solar Phys.*, *230*(1), 7–25.

Schonfeld, S. J., S. M. White, C. J. Henney, C. N. Arge, and R. T. J. McAteer (2015), Coronal sources of the solar F10.7 radio flux, *Astrophy. J.*, *808*(1).

Schunk, R. W., L. Scherliess, J. J. Sojka, D. C. Thompson, D. N. Anderson, M. Codrescu, C. Minter, T. J. Fuller-Rowell, R. A. Heelis, M. Hairston, and B. M. Howe (2004), Global assimilation of ionospheric measurements (gaim), *Radio Sci.*, *39*, doi: 10.1029/2002RS002794.

Schunk, R. W., L. Scherliess, J. J. Sojka, D. C. Thompson, and L. Zhu (2005), Ionospheric weather forecasting on the horizon, *Space Weather*, *3*(S08007), doi:10.1029/2004SW000138.

Schunk, R. W., L. Gardner, L. Scherliess, and L. Zhu (2012), Problems associated with uncertain parameters and missing physics for long-term ionosphere-thermosphere forecasting, *Radio Sci.*, *47*(RS0L23), doi:10.1029/2011RS004911.

Schunk, R. W., L. Scherliess, V. Eccles, L. C. Gardner, J. J. Sojka, L. Zhu, X. Pi, A. J. Mannucci, B. D. Wilson, A. Komjathy, C. Wang, and G. Rosen (2014), Ensemble modeling with data assimilation models: A new strategy for space weather specifications, forecasts, and science, *Space Weather*, *12*, 123–126, doi:10.1002/2014SW001050.

Shim, J. S., L. Rastatter, M. Kuznetsova, D. Bilitza, M. Codrescu, A. J. Coster, B. A. Emery, M. Fedrizzi, M. Forster, T. J. Fuller-Rowell, L. C. Gardner, L. Goncharenko, J. Huba, S. E. McDonald, A. J. Mannucci, A. A. Namgaladze, X. Pi, B. E. Prokhorov, A. J. Ridley, L. Scherliess, R. W. Schunk, J. Sojka, and L. Zhu (2017), CEDAR-GEM challenge for systematic assessment of ionosphere/thermosphere models in predicting TEC during the 2006 December storm event, *Space Weather*, *15*, 1238–1256.

Shim, J. S., I. Tsagouri, L. Goncharenko, L. Rastaetter, M. Kuznetsova, D. Bilitza, M. Codrescu, A. J. Coster, S. C. Solomon, M. Fedrizzi, M. Forster, T. J. Fuller-Rowell, L. C. Gardner, J. Huba, A. A. Namgaladze, B. E. Prokhorov, A. J. Ridley, L. Scherliess, R. W. Schunk, J. Sojka, and L. Zhu (2018), Validation of ionospheric specifications during geomagnetic storms: TEC and foF2 during the 2013 March storm event, *Space Weather*, *16*, 1686–1701.

Shiokawa, K., G. Lu, Y. Otsuka, T. Ogawa, M. Yamamoto, N. Nishitani, and N. Sato (2007), Ground observation and AMIE-TIEGCM modeling of a storm-time traveling ionospheric disturbance, *J. Geophys. Res.*, *112*(A05308).

Solomon, S. C., and L. Qian (2005), Solar extreme-ultraviolet irradiance for general circulation models, *J. Geophys. Res.*, *110*(A10306), doi:10.1029/2005JA011160.

Solomon, S. C., L. Qian, L. V. Didkovsky, R. A. Viereck, and T. N. Woods (2011), Causes of low thermospheric density during the 2007-2009 solar minimum, *Journal of Geophysical Research: Space Physics*, *116*(A2), doi:10.1029/2011JA016508.

Solomon, S. C., A. G. Burns, B. A. Emery, M. G. Mlynczak, L. Qian, W. Wang, D. R. Weimer, and M. Wiltberger (2012), Modeling studies of the impact of high-speed streams and co-rotating interaction regions on the thermosphere-ionosphere, *J. Geophys. Res.*, *117*(A00L11), doi:10.1029/2011JA017417.

Tapping, K. F. (2013), The 10.7 cm solar radio flux (F10.7), *Space Weather*, *11*, 394–406.

Tapping, K. F., and D. P. Charrois (1994), Limits to the accuracy of the 10.7 cm flux, *Solar Physics*, *150*, 305–315.

Tobiska, W. K. (1991), Revised solar extreme ultraviolet flux model, *J. Atmos. Solar-Terr. Phys.*, *53*, 1005.

Tobiska, W. K. (1996), Current status of solar EUV measurements and modeling, *Adv. Space Res.*, *18*(3).

Tsurutani, B. T., W. D. Gonzalez, A. L. C. Gonzalez, F. L. Guarnieri, N. Gopalswamy, M. Grande, Y. Kamide, Y. Kasahara, G. Lu, I. Mann, R. McPherron, F. Soraas, and V. Vasyliunas (2006), Corotating solar wind streams and recurrent geomagnetic activity: A review, *J. Geophys. Res.*, *111*(A07S01), doi:10.1029/2005JA011273.

Verkhoglyadova, O., X. Meng, A. J. Mannucci, B. T. Tsurutani, L. A. Hunt, M. G. Mlynczak, R. Hajra, and B. A. Emery (2016), Estimation of energy budget of ionosphere-thermosphere system during two CIR-HSS events: observations and modeling, *J. Space Weather Space Clim.*, *6*(A20).

Vichare, G., A. Ridley, and E. Yiğit (2012), Quiet-time low latitude ionospheric electrodynamics in the non-hydrostatic Global Ionosphere-Thermosphere Model, *J. Atmos. Solar-Terr. Phys.*, *80*, 167–172.

Viereck, R., L. Puga, D. McMullin, D. Judge, M. Weber, and W. K. Tobiska (2001), The Mg II index: A proxy for solar EUV, *Geophys. Res. Lett.*, *28*, 1343–1346.

Wang, W., J. Lei, A. G. Burns, M. Wiltberger, A. D. Richmond, S. C. Solomon, T. L. Killeen, E. R. Talaat, and D. N. Anderson (2008), Ionospheric electric field variations during a geomagnetic storm simulated by a coupled magnetosphere ionosphere thermosphere (CMIT) model, *Geophys. Res. Lett.*, *35*(L18105), doi:10.1029/2008GL035155.

Warren, H. P., J. T. Emmert, and N. A. Crump (2017), Linear forecasting of the F10.7 proxy for solar activity, *Space Weather*, *15*, 1039–1051.

Weimer, D. R. (2005a), Improved ionospheric electrodynamic models and application to calculating Joule heating rates, *J. Geophys. Res.*, *110*(A05306), doi:10.1029/2004JA010884.

Weimer, D. R. (2005b), Predicting surface geomagnetic variations using ionospheric electrodynamic models, *J. Geophys. Res.*, *110*(A12307), doi:10.1029/2005JA011270.

Wintoft, P. (2011), The variability of solar EUV: A multiscale comparison between sunspot number, 10.7 cm flux, LASP MgII index, and SOHO/SEM EUV flux, *J. Atmos. Solar-Terr. Phys.*, *73*, 1708–1714.

Woods, T. N., and G. J. Rottman (2002), Solar ultraviolet variability over time periods of aeronomic interest, in *Comparative aeronomy in the solar system*, vol. 130, edited by M. Mendillo, A. Nagy, and J. Waite, Washington, D.C.

Woods, T. N., F. G. Eparvier, S. M. Bailey, P. C. Chamberlin, J. Lean, G. J. Rottman, S. C. Solomon, W. K. Tobiska, and D. L. Woodraska (2005), The Solar EUV Experiment (SEE): Mission overview and first results, *J. Geophys. Res.*, *110*, A01,312, doi:10.1029/2004JA010765.

Yasyukevich, Y. V., E. Afraimovich, K. Palamartchouk, and P. Tatarinov (2010), Cross testing of ionosphere models iri-2001 and iri-2007, data from satellite altimeters (topex/poseidon and jason-1) and global ionosphere maps, *Advances in Space Research*, *46*, 990–1007, doi:10.1016/j.asr.2010.06.010.

Yu, Y., V. K. Jordanova, A. J. Ridley, G. Toth, and R. Heelis (2017), Effects of electric field methods on modeling the midlatitude ionospheric electrodynamics and inner magnetosphere dynamics, *J. Geophys. Res.*, *122*, 5321–5338, doi:10.1002/2016JA023850.

Zhu, Q., Y. Deng, A. Maute, C. Sheng, and C. Y. Lin (2017), Impact of the vertical dynamics on the thermosphere at low and middle latitudes: GITM simulations, *J. Geophys. Res.*, *122*, 6882–6891, doi:10.1002/2017JA023939.

Figure 1.

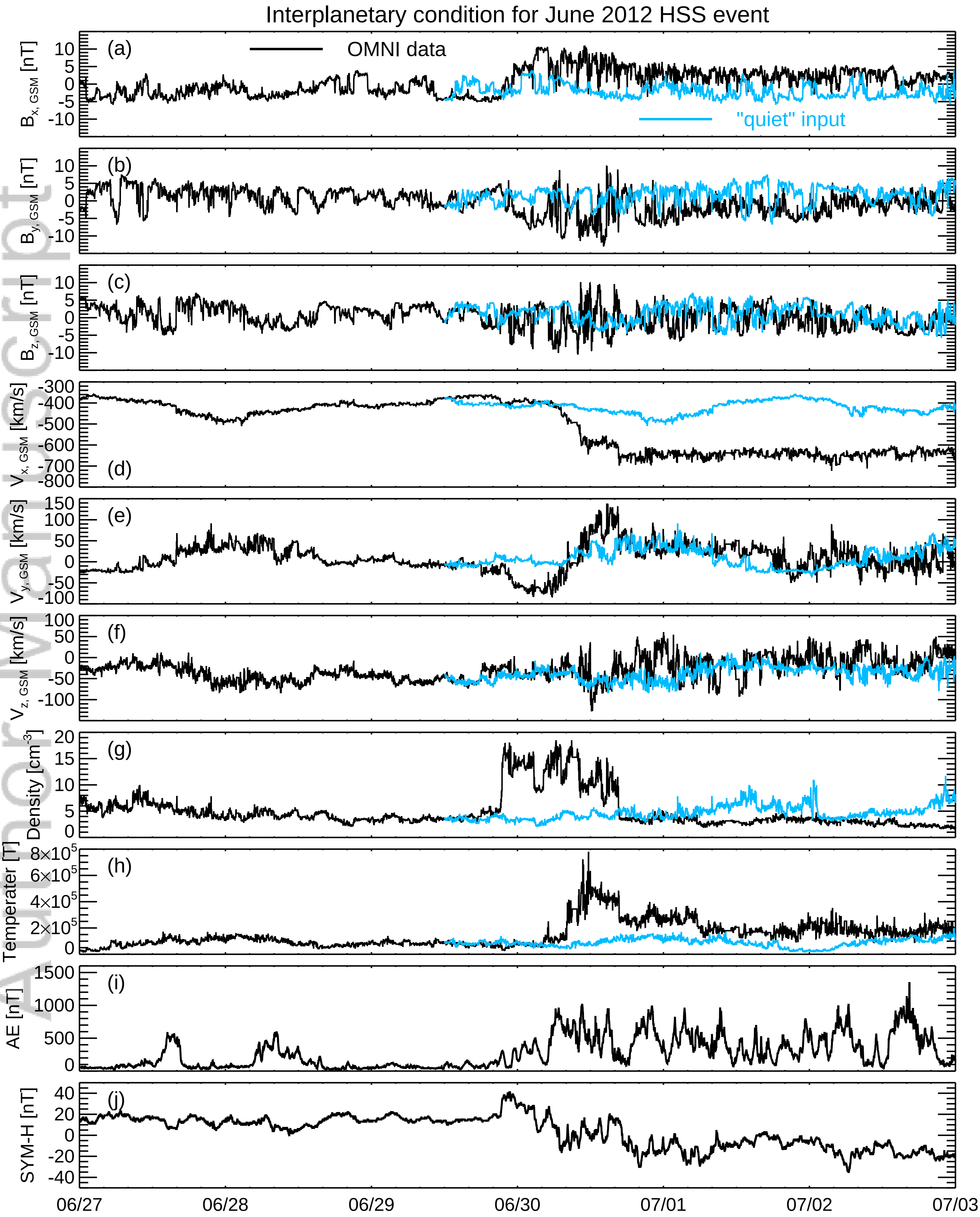
Interplanetary condition for June 2012 HSS event
(a)
OMNI data
"quiet" input
$B_{x,\ GSM}$ [nT]
(b)
$B_{y,\ GSM}$ [nT]
(c)
$B_{z,\ GSM}$ [nT]
(d)
$V_{x,\ GSM}$ [km/s]
(e)
$V_{y,\ GSM}$ [km/s]
(f)
$V_{z,\ GSM}$ [km/s]
(g)
Density [cm^{-3}]
(h)
Temperater [T]
(i)
AE [nT]
(j)
SYM-H [nT]
06/27
06/28
06/29
06/30
07/01
07/02
07/03
Date in 2012

Figure 2.

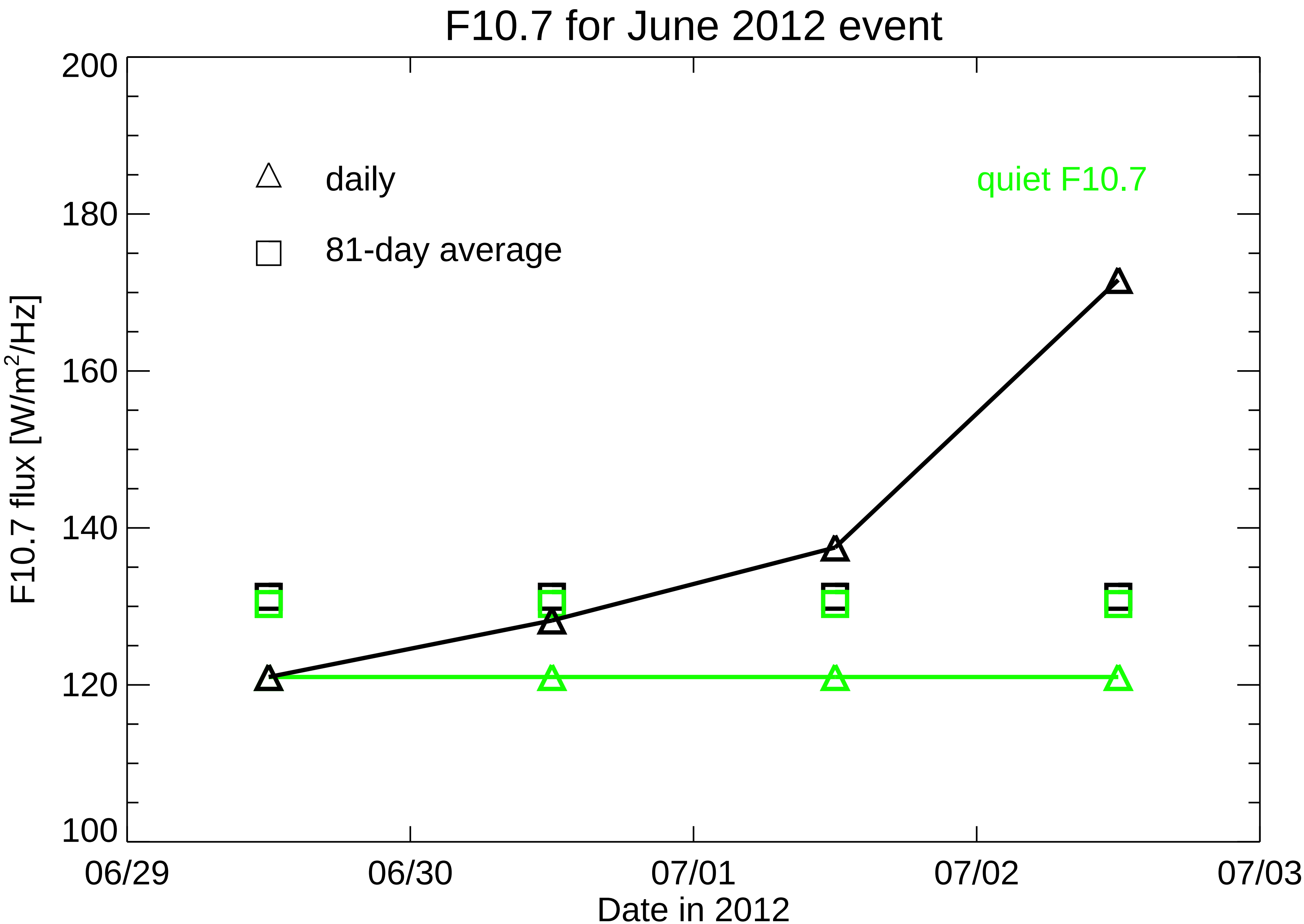
F10.7 for June 2012 event
daily
81-day average
quiet F10.7
F10.7 flux [W/m2/Hz]
200
180
160
140
120
100
06/29
06/30
07/01
07/02
07/03
Date in 2012

Figure 3.

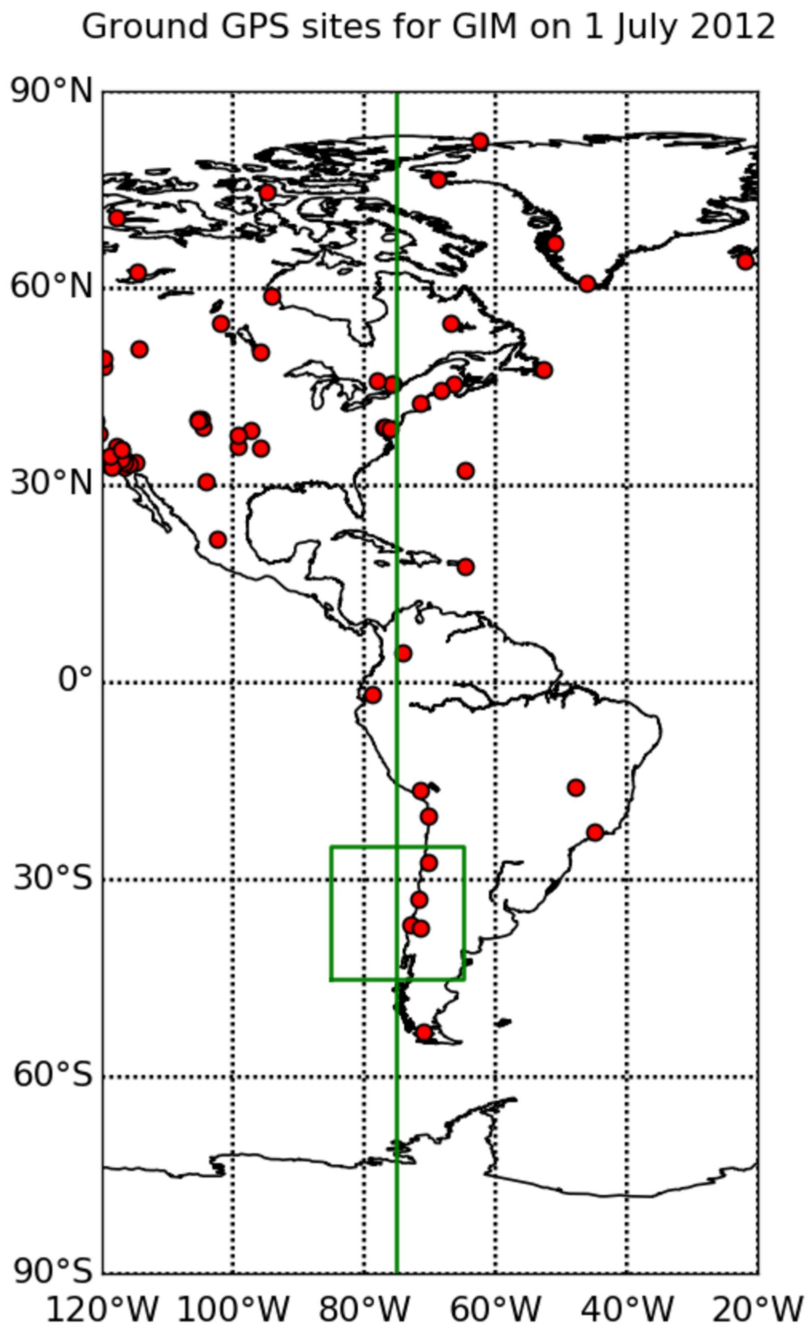
Ground GPS sites for GIM on 1 July 2012
90°N
60°N
30°N
0°
30°S
60°S
90°S
120°W
100°W
80°W
60°W
40°W
20°W

Figure 4.

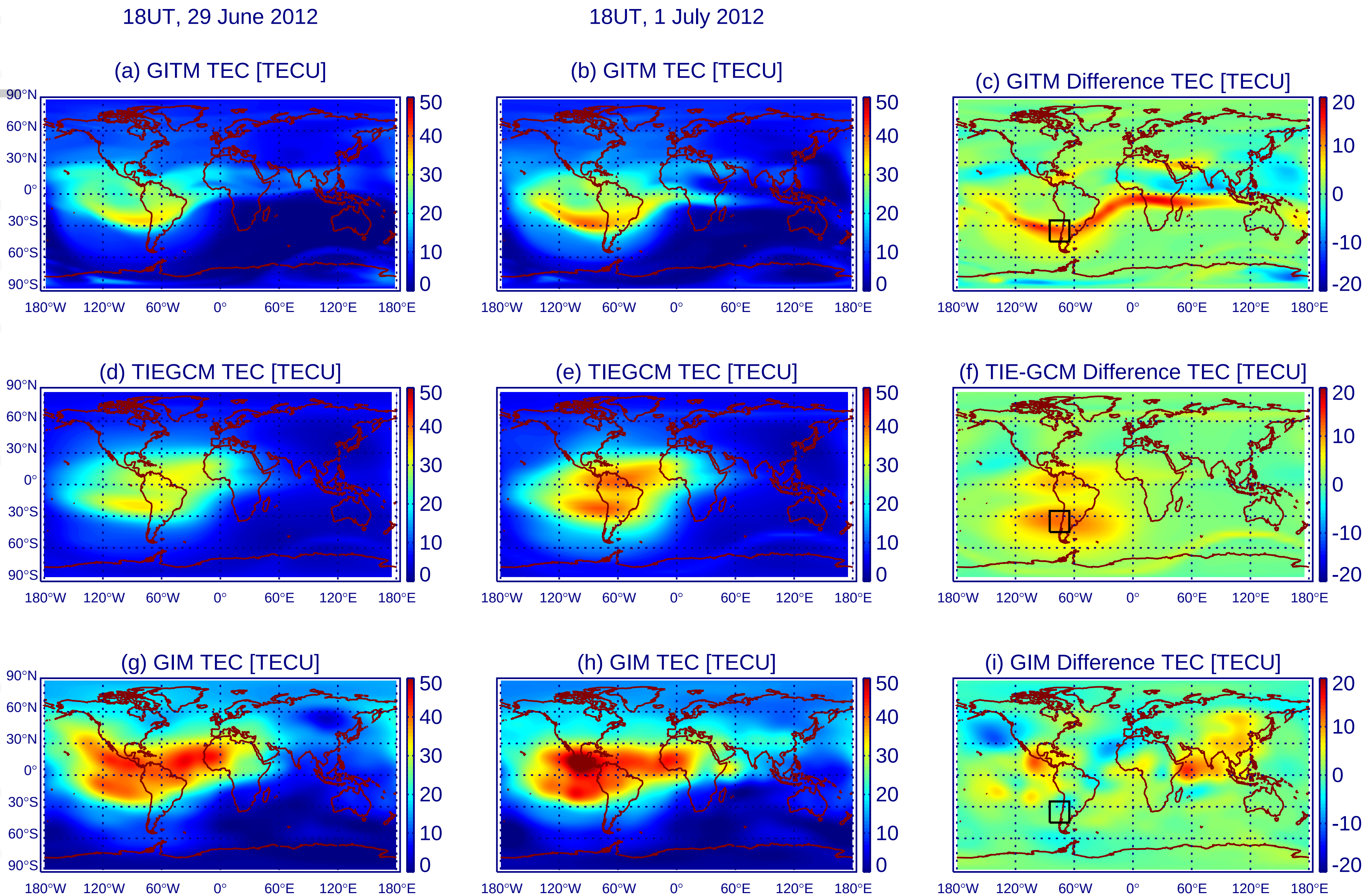

18UT, 29 June 2012
18UT, 1 July 2012
(a) GITM TEC [TECU]
(b) GITM TEC [TECU]
(c) GITM Difference TEC [TECU]
(d) TIEGCM TEC [TECU]
(e) TIEGCM TEC [TECU]
(f) TIE-GCM Difference TEC [TECU]
(g) GIM TEC [TECU]
(h) GIM TEC [TECU]
(i) GIM Difference TEC [TECU]
90°N
60°N
30°N
0°
30°S
60°S
90°S
180°W
120°W
60°W
0°
60°E
120°E
180°E
50
40
30
20
10
0
20
10
0
-10
-20

Figure 5.

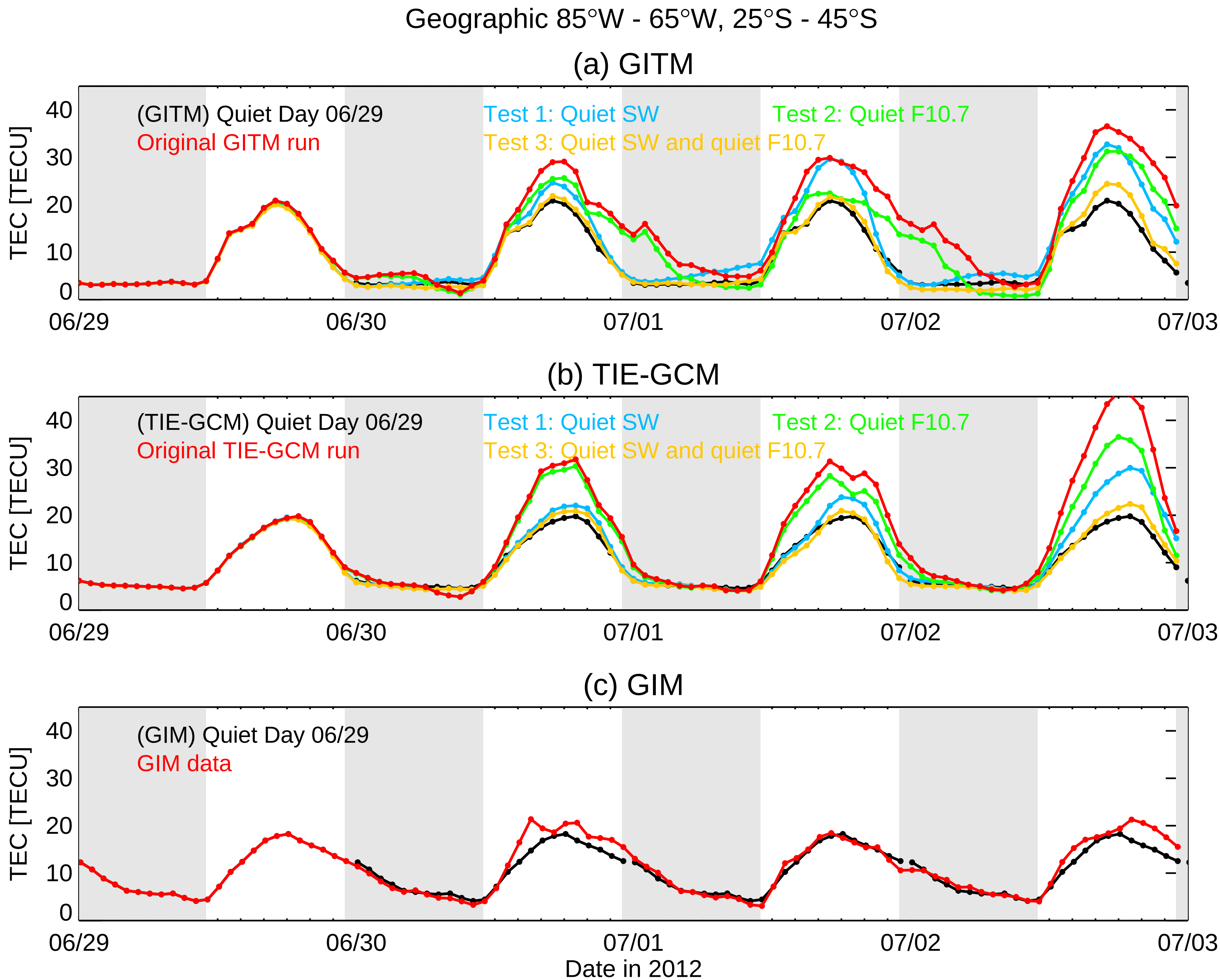
Geographic 85°W - 65°W, 25°S - 45°S
(a) GITM
(GITM) Quiet Day 06/29
Original GITM run
Test 1: Quiet SW
Test 2: Quiet F10.7
Test 3: Quiet SW and quiet F10.7
TEC [TECU]
0
10
20
30
40
06/29
06/30
07/01
07/02
07/03
(b) TIE-GCM
(TIE-GCM) Quiet Day 06/29
Original TIE-GCM run
Test 1: Quiet SW
Test 2: Quiet F10.7
Test 3: Quiet SW and quiet F10.7
(c) GIM
(GIM) Quiet Day 06/29
GIM data
Date in 2012

Figure 6.

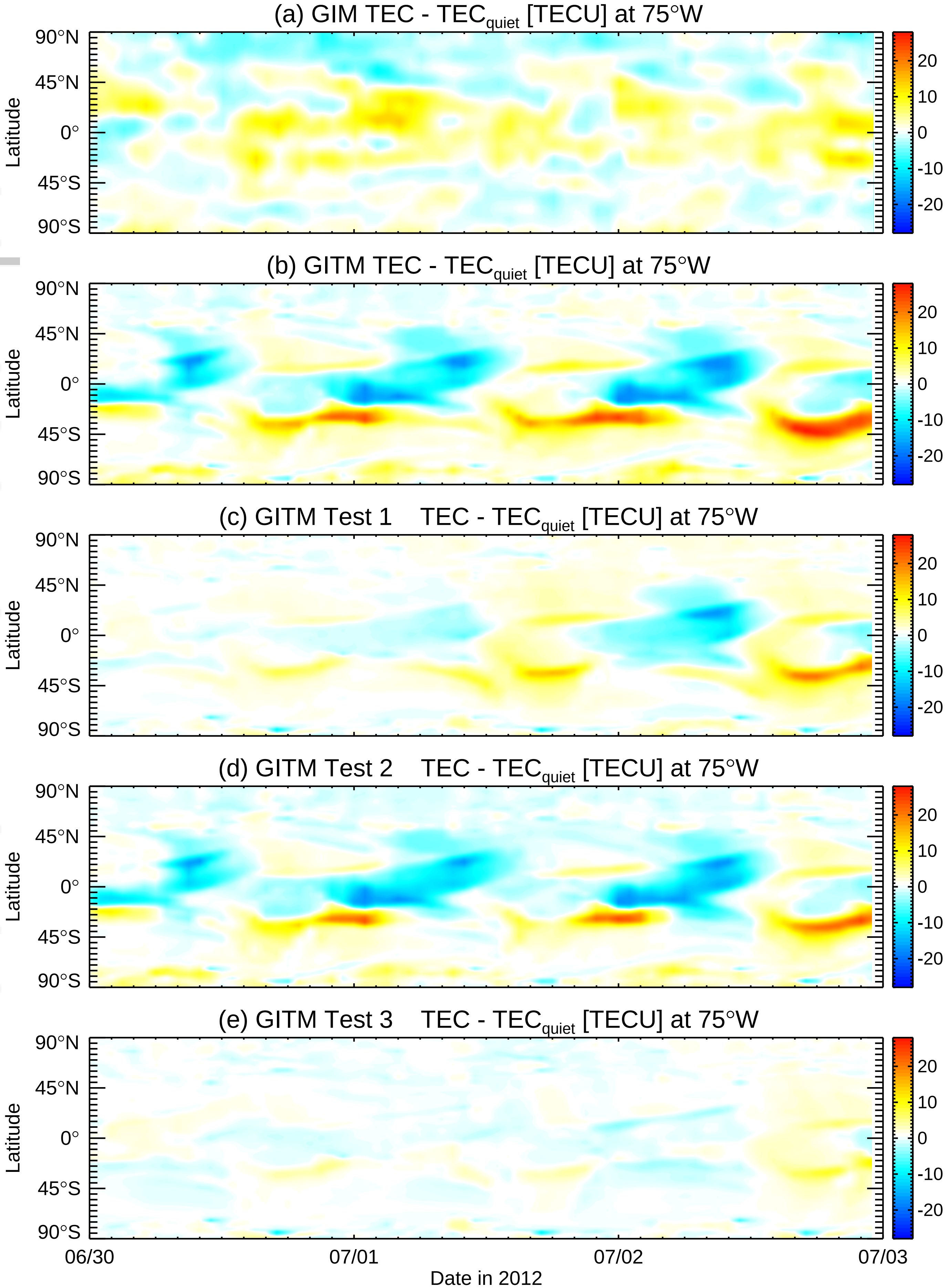

(a) GIM TEC - TEC$_{quiet}$ [TECU] at 75°W
(b) GITM TEC - TEC$_{quiet}$ [TECU] at 75°W
(c) GITM Test 1 TEC - TEC$_{quiet}$ [TECU] at 75°W
(d) GITM Test 2 TEC - TEC$_{quiet}$ [TECU] at 75°W
(e) GITM Test 3 TEC - TEC$_{quiet}$ [TECU] at 75°W
Latitude
90°N
45°N
0°
45°S
90°S
20
10
0
-10
-20
06/30
07/01
07/02
07/03
Date in 2012

Figure 7.

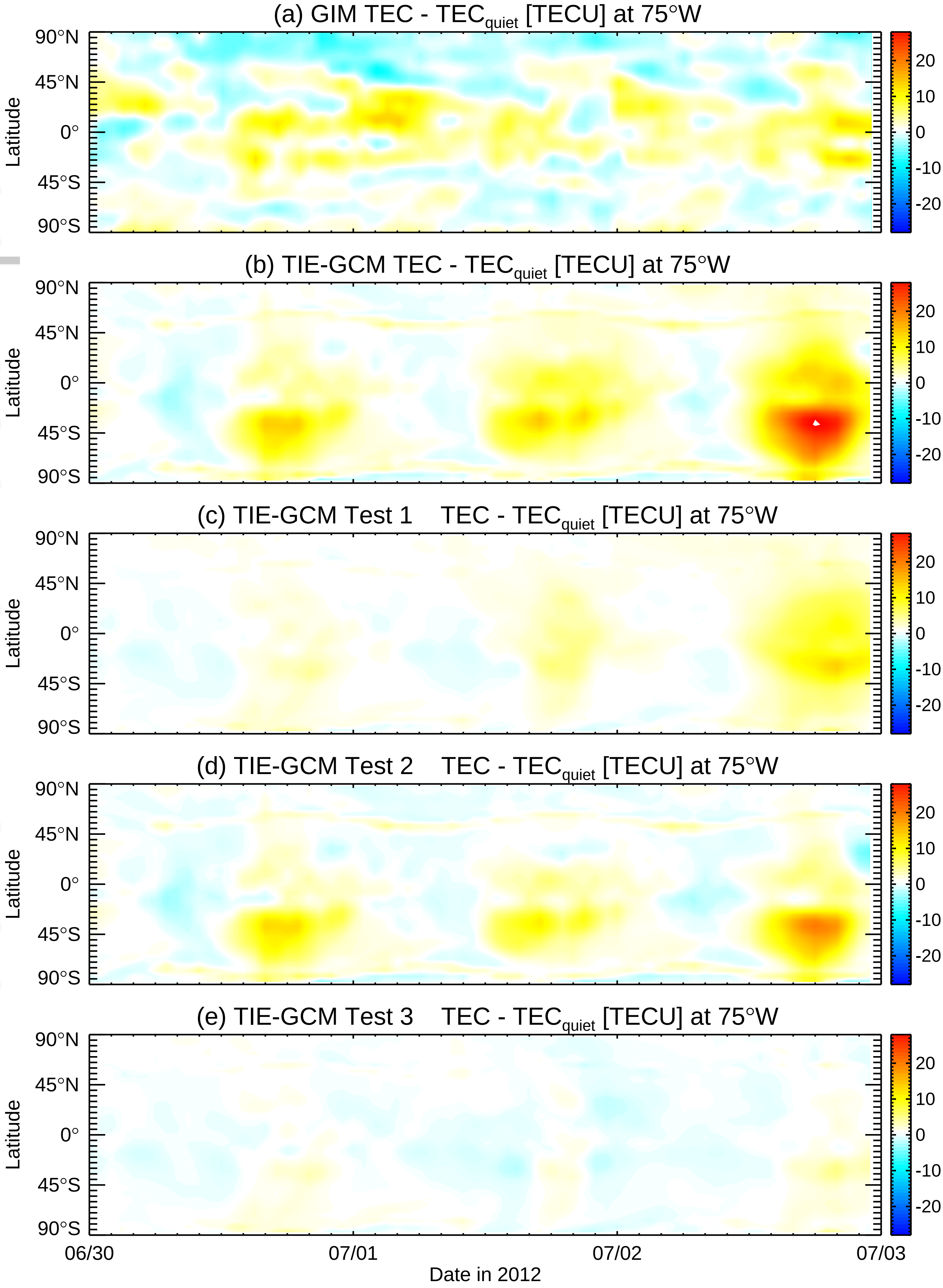

(a) GIM TEC - TEC$_{quiet}$ [TECU] at 75°W
(b) TIE-GCM TEC - TEC$_{quiet}$ [TECU] at 75°W
(c) TIE-GCM Test 1 TEC - TEC$_{quiet}$ [TECU] at 75°W
(d) TIE-GCM Test 2 TEC - TEC$_{quiet}$ [TECU] at 75°W
(e) TIE-GCM Test 3 TEC - TEC$_{quiet}$ [TECU] at 75°W
90°N
45°N
0°
45°S
90°S
Latitude
20
10
0
-10
-20
06/30
07/01
07/02
07/03
Date in 2012

Figure 8.

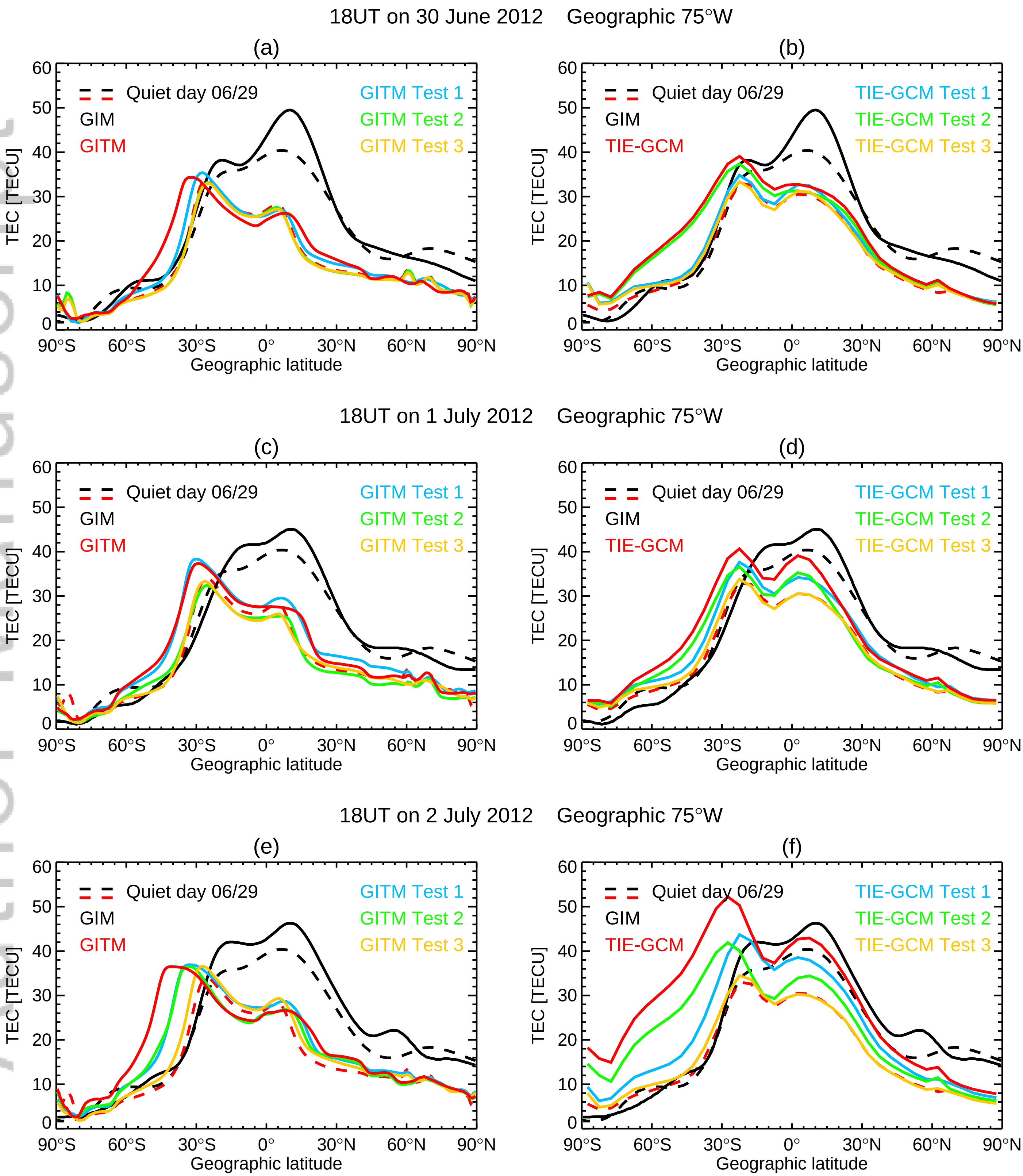

18UT on 30 June 2012 Geographic 75°W
(a)
(b)
Quiet day 06/29
GIM
GITM
GITM Test 1
GITM Test 2
GITM Test 3
TIE-GCM
TIE-GCM Test 1
TIE-GCM Test 2
TIE-GCM Test 3
TEC [TECU]
Geographic latitude
90°S 60°S 30°S 0° 30°N 60°N 90°N
0 10 20 30 40 50 60
18UT on 1 July 2012 Geographic 75°W
(c)
(d)
18UT on 2 July 2012 Geographic 75°W
(e)
(f)

Figure 9.

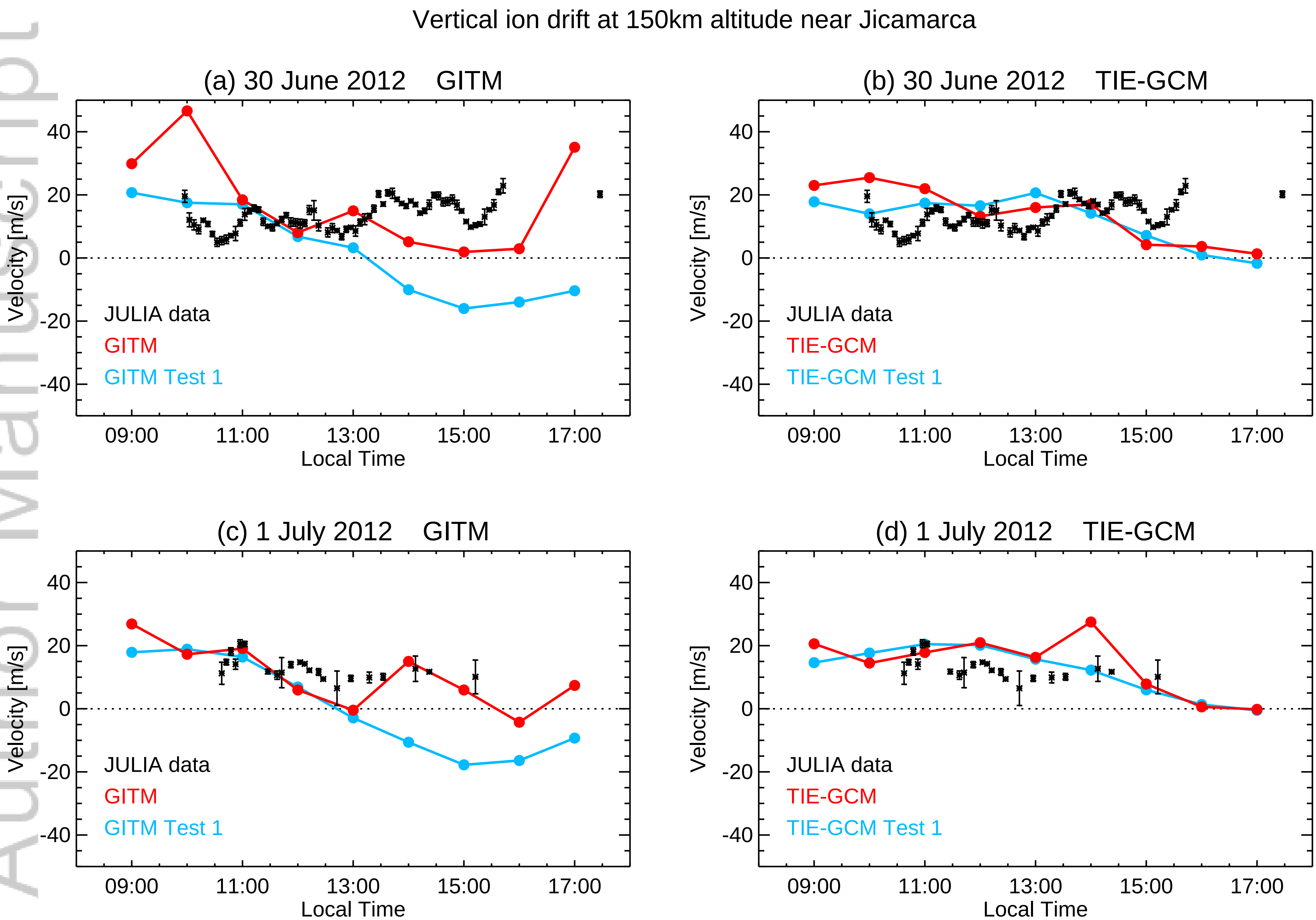
Vertical ion drift at 150km altitude near Jicamarca
(a) 30 June 2012 GITM
(b) 30 June 2012 TIE-GCM
(c) 1 July 2012 GITM
(d) 1 July 2012 TIE-GCM
Velocity [m/s]
Local Time
40
20
0
-20
-40
09:00
11:00
13:00
15:00
17:00
JULIA data
GITM
GITM Test 1
TIE-GCM
TIE-GCM Test 1

Figure 10.

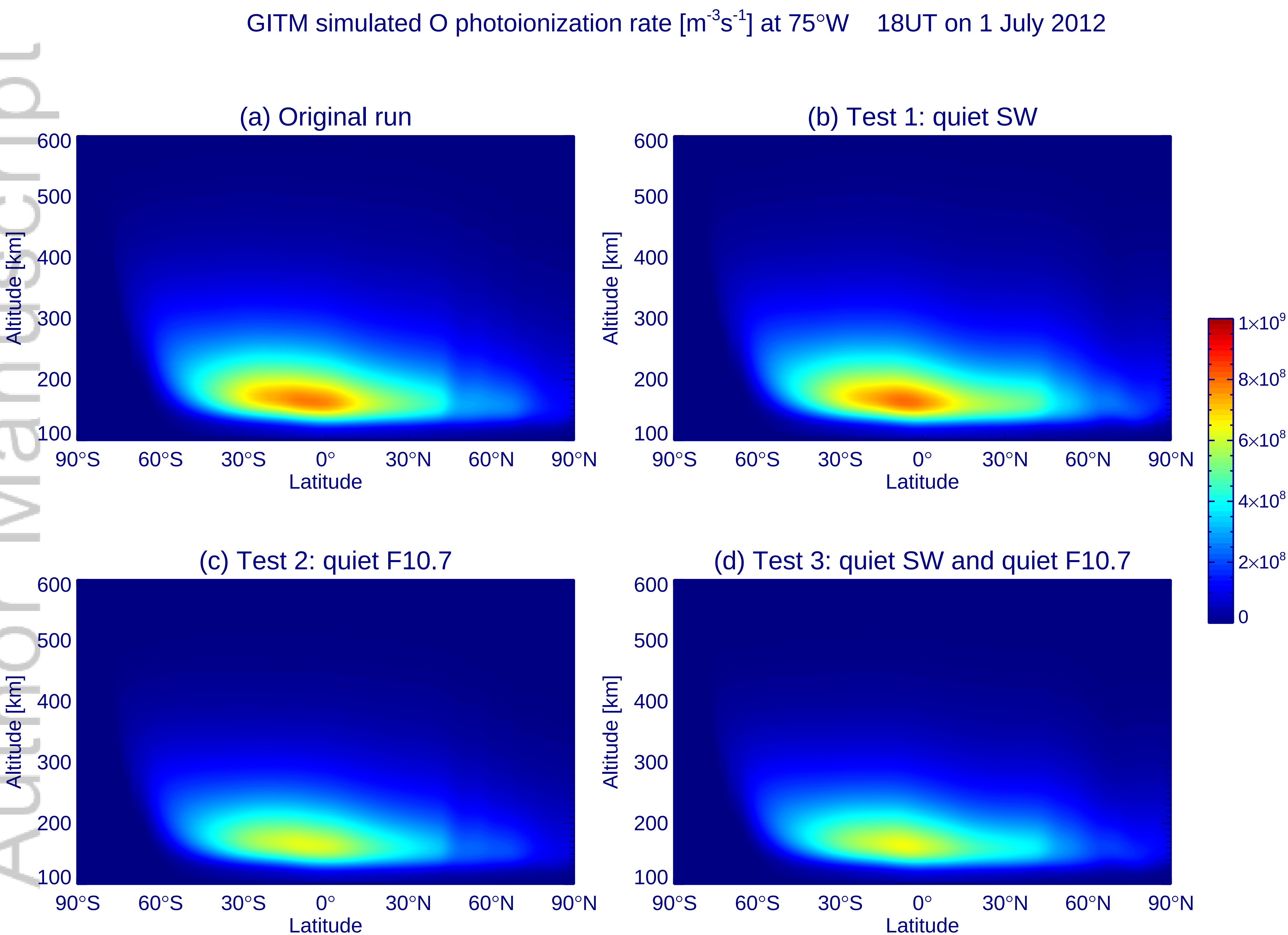
GITM simulated O photoionization rate [m-3s-1] at 75°W 18UT on 1 July 2012
(a) Original run
(b) Test 1: quiet SW
(c) Test 2: quiet F10.7
(d) Test 3: quiet SW and quiet F10.7
Altitude [km]
100
200
300
400
500
600
Latitude
90°S
60°S
30°S
0°
30°N
60°N
90°N
0
2×10^8
4×10^8
6×10^8
8×10^8
1×10^9

Figure 11.

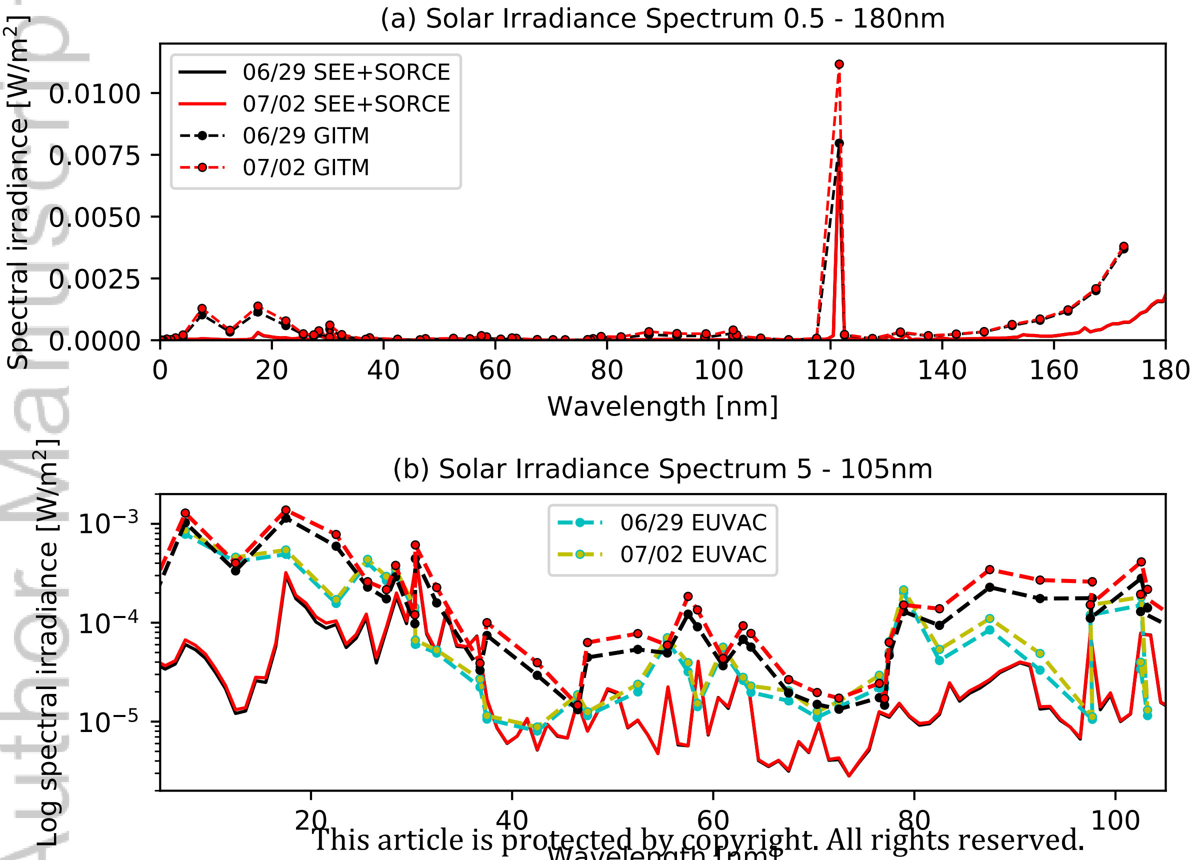
(a) Solar Irradiance Spectrum 0.5 - 180nm
06/29 SEE+SORCE
07/02 SEE+SORCE
06/29 GITM
07/02 GITM
Spectral irradiance [W/m²]
Wavelength [nm]
(b) Solar Irradiance Spectrum 5 - 105nm
06/29 EUVAC
07/02 EUVAC
Log spectral irradiance [W/m²]
Wavelength [nm]

Figure 12.

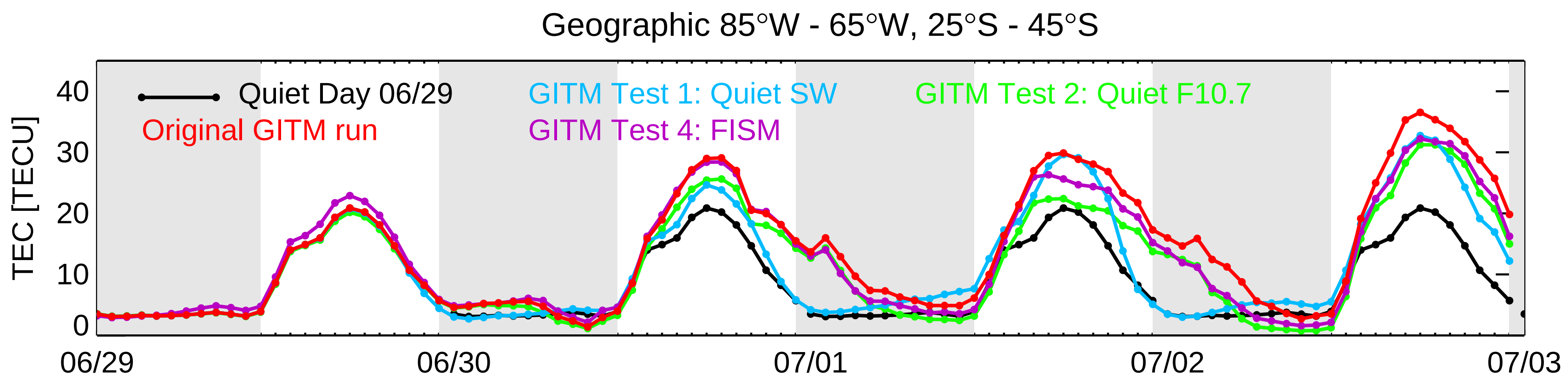
Geographic 85°W - 65°W, 25°S - 45°S
Quiet Day 06/29
Original GITM run
GITM Test 1: Quiet SW
GITM Test 4: FISM
GITM Test 2: Quiet F10.7
TEC [TECU]
0
10
20
30
40
06/29
06/30
07/01
07/02
07/03

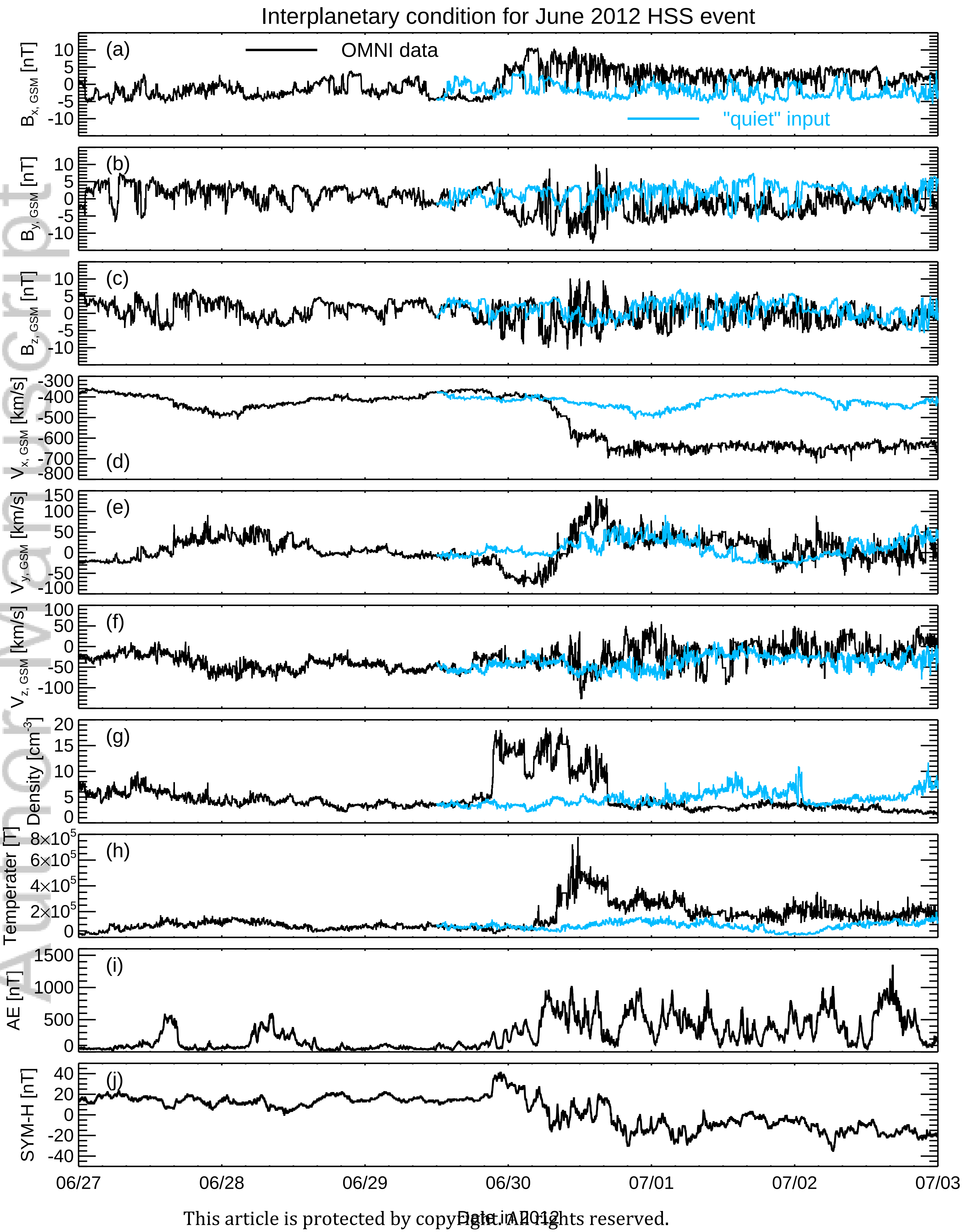

Interplanetary condition for June 2012 HSS event
OMNI data
"quiet" input
Bx, GSM [nT]
By, GSM [nT]
Bz, GSM [nT]
Vx, GSM [km/s]
Vy, GSM [km/s]
Vz, GSM [km/s]
Density [cm-3]
Temperater [T]
AE [nT]
SYM-H [nT]
(a)
(b)
(c)
(d)
(e)
(f)
(g)
(h)
(i)
(j)
06/27
06/28
06/29
06/30
07/01
07/02
07/03
Date in 2012

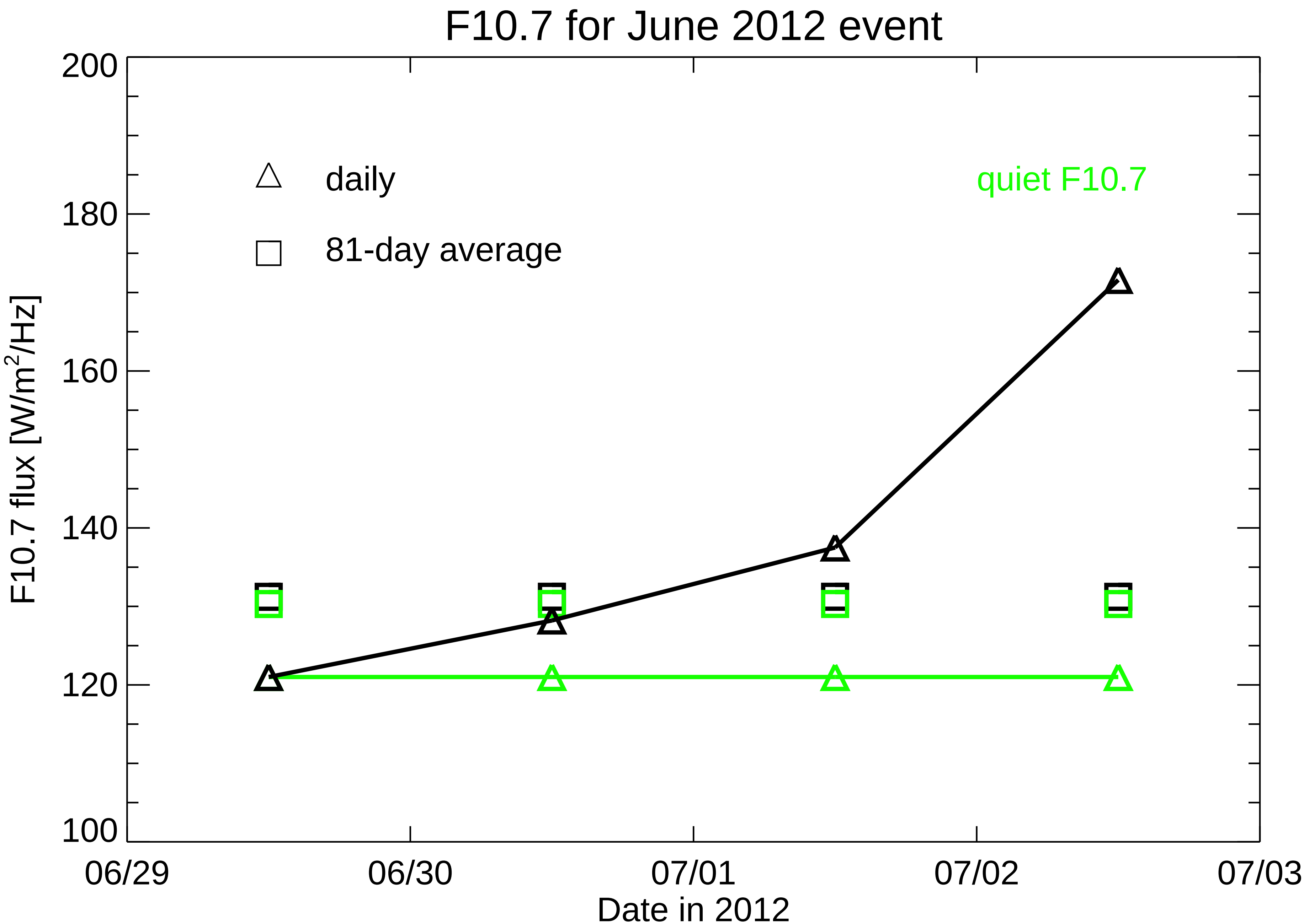
F10.7 for June 2012 event
daily
81-day average
quiet F10.7
F10.7 flux [W/m2/Hz]
200
180
160
140
120
100
06/29
06/30
07/01
07/02
07/03
Date in 2012

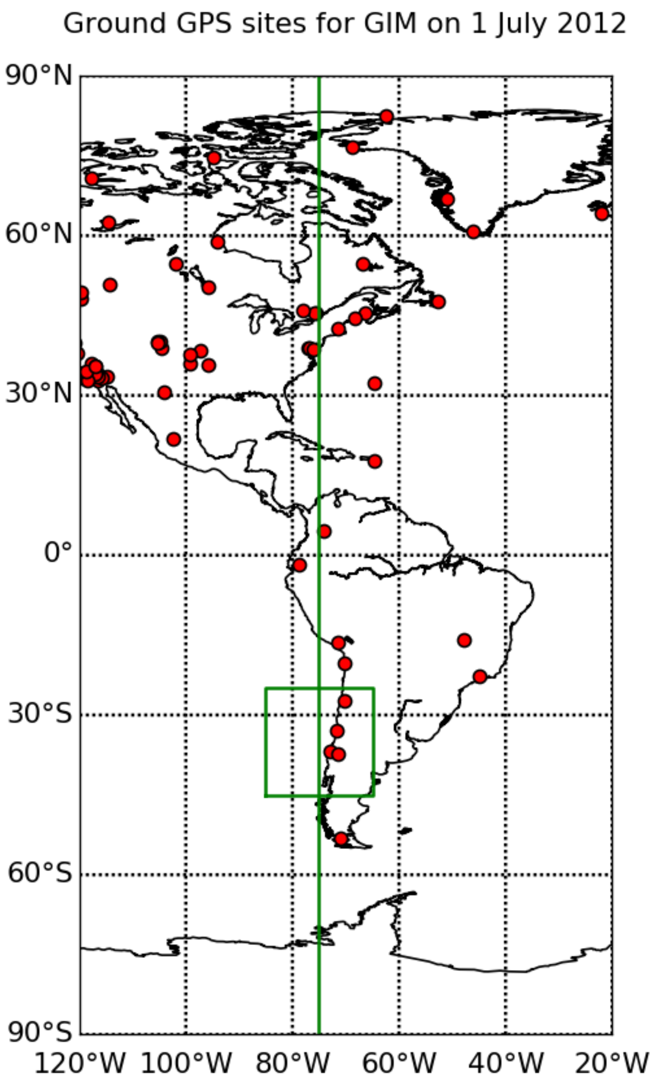

2019SW002352-f03-z-.png

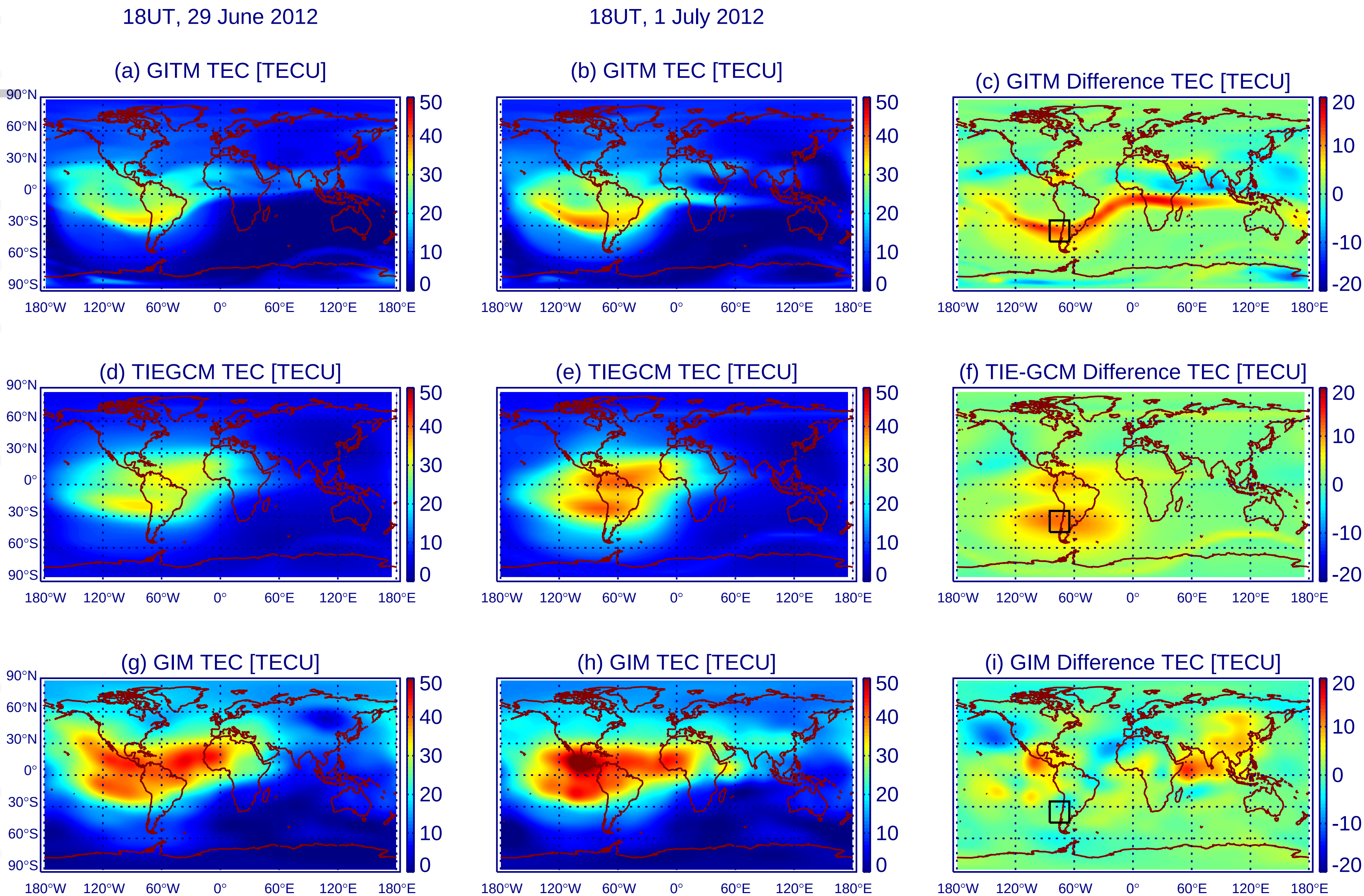
18UT, 29 June 2012
18UT, 1 July 2012
(a) GITM TEC [TECU]
(b) GITM TEC [TECU]
(c) GITM Difference TEC [TECU]
(d) TIEGCM TEC [TECU]
(e) TIEGCM TEC [TECU]
(f) TIE-GCM Difference TEC [TECU]
(g) GIM TEC [TECU]
(h) GIM TEC [TECU]
(i) GIM Difference TEC [TECU]
90°N
60°N
30°N
0°
30°S
60°S
90°S
180°W
120°W
60°W
0°
60°E
120°E
180°E
50
40
30
20
10
0
20
10
0
-10
-20

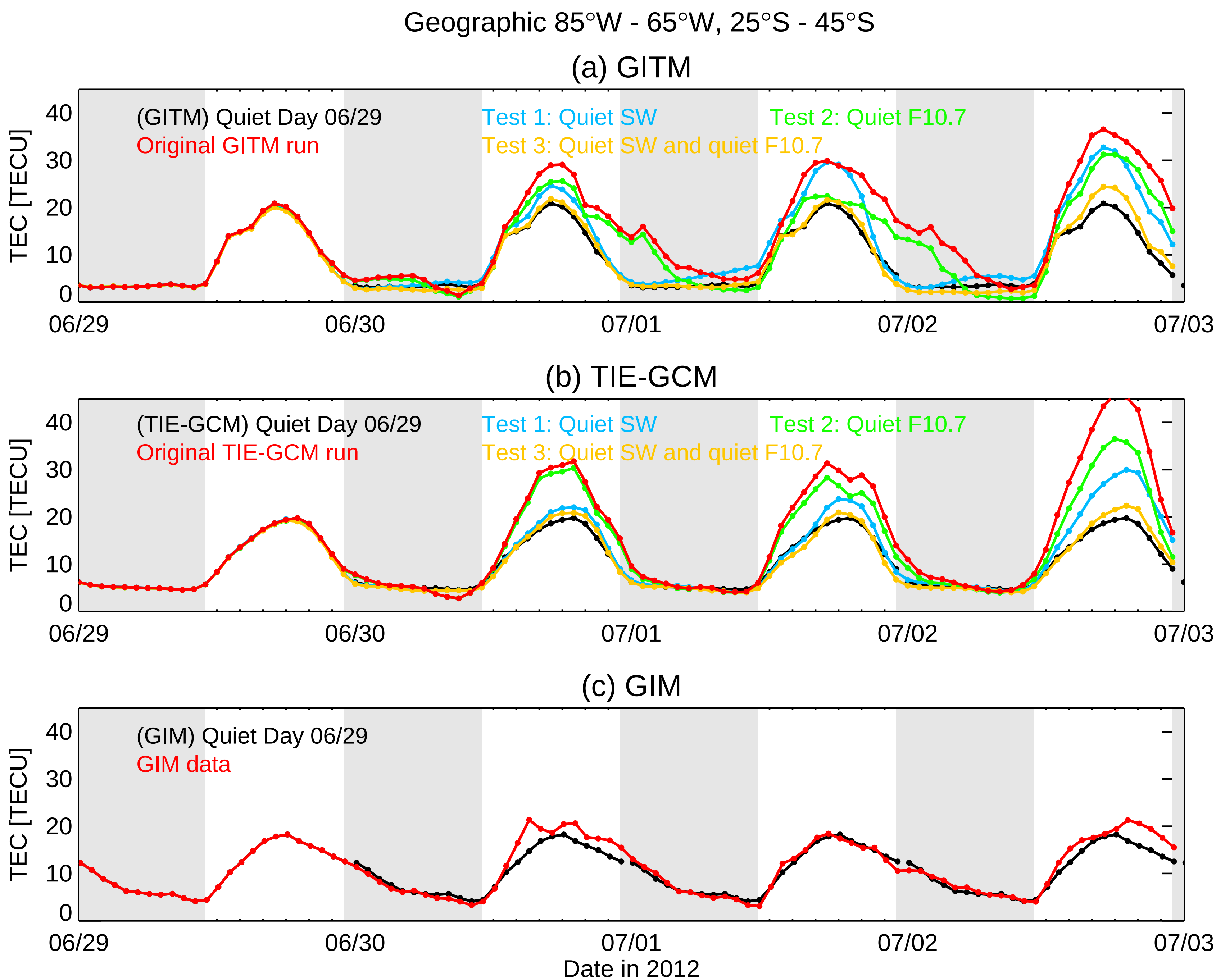

Geographic 85°W - 65°W, 25°S - 45°S
(a) GITM
(GITM) Quiet Day 06/29
Original GITM run
Test 1: Quiet SW
Test 2: Quiet F10.7
Test 3: Quiet SW and quiet F10.7
TEC [TECU]
40
30
20
10
0
06/29
06/30
07/01
07/02
07/03
(b) TIE-GCM
(TIE-GCM) Quiet Day 06/29
Original TIE-GCM run
Test 1: Quiet SW
Test 2: Quiet F10.7
Test 3: Quiet SW and quiet F10.7
(c) GIM
(GIM) Quiet Day 06/29
GIM data
Date in 2012

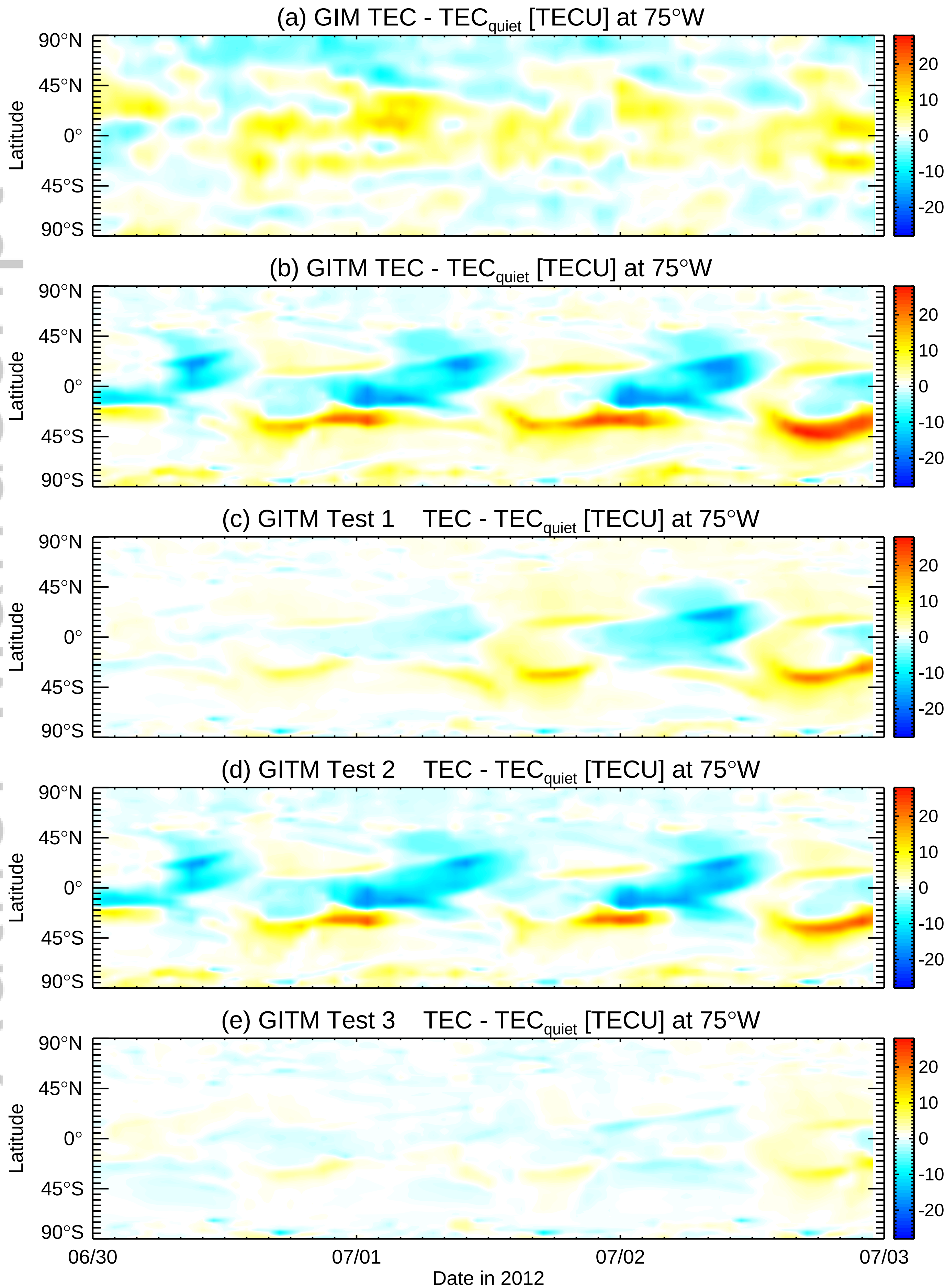
(a) GIM TEC - TEC$_{quiet}$ [TECU] at 75°W
(b) GITM TEC - TEC$_{quiet}$ [TECU] at 75°W
(c) GITM Test 1 TEC - TEC$_{quiet}$ [TECU] at 75°W
(d) GITM Test 2 TEC - TEC$_{quiet}$ [TECU] at 75°W
(e) GITM Test 3 TEC - TEC$_{quiet}$ [TECU] at 75°W
Latitude
90°N
45°N
0°
45°S
90°S
20
10
0
-10
-20
06/30
07/01
07/02
07/03
Date in 2012

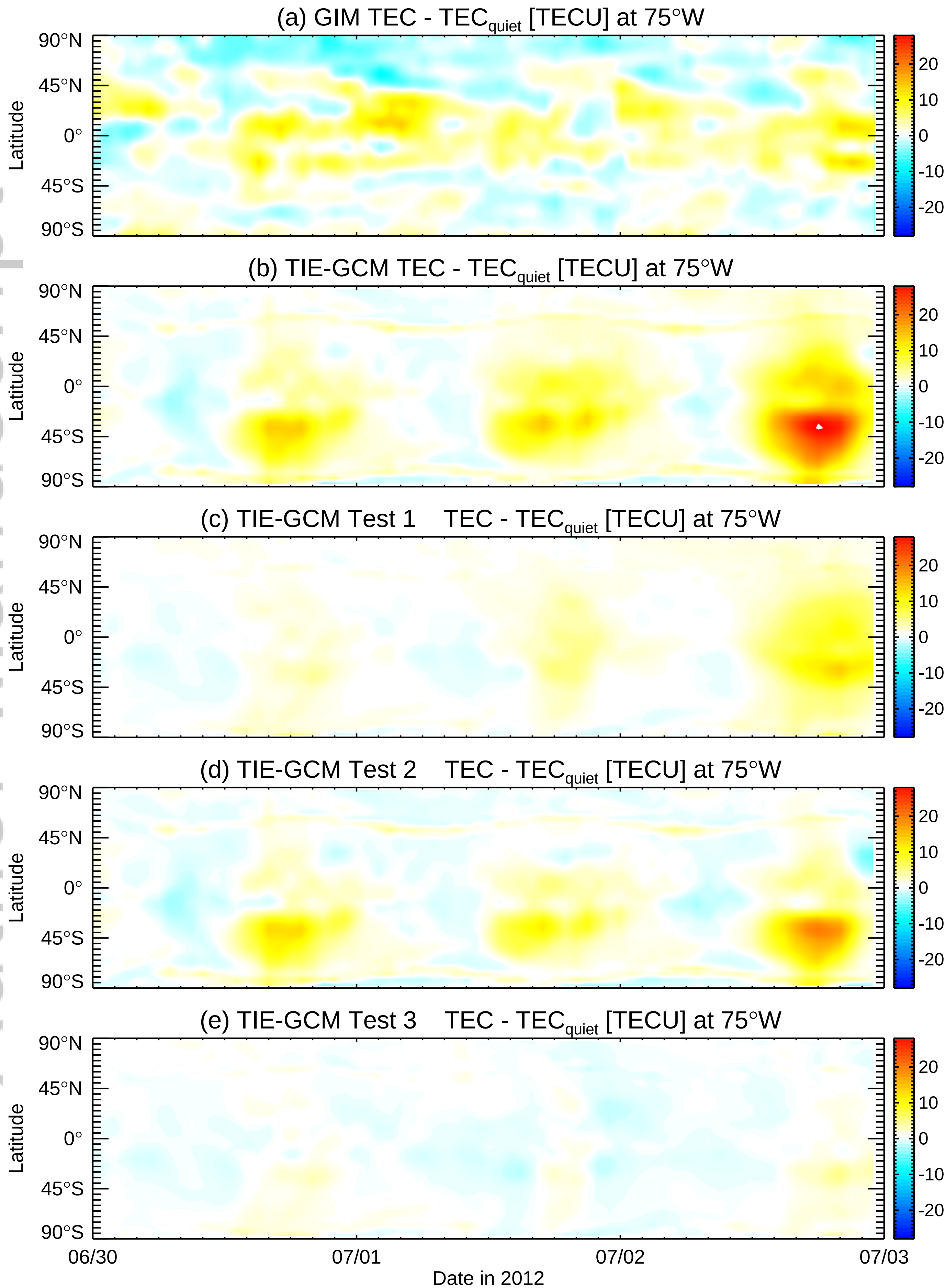
(a) GIM TEC - TEC$_{quiet}$ [TECU] at 75°W
(b) TIE-GCM TEC - TEC$_{quiet}$ [TECU] at 75°W
(c) TIE-GCM Test 1 TEC - TEC$_{quiet}$ [TECU] at 75°W
(d) TIE-GCM Test 2 TEC - TEC$_{quiet}$ [TECU] at 75°W
(e) TIE-GCM Test 3 TEC - TEC$_{quiet}$ [TECU] at 75°W
Latitude
90°N
45°N
0°
45°S
90°S
20
10
0
-10
-20
06/30
07/01
07/02
07/03
Date in 2012

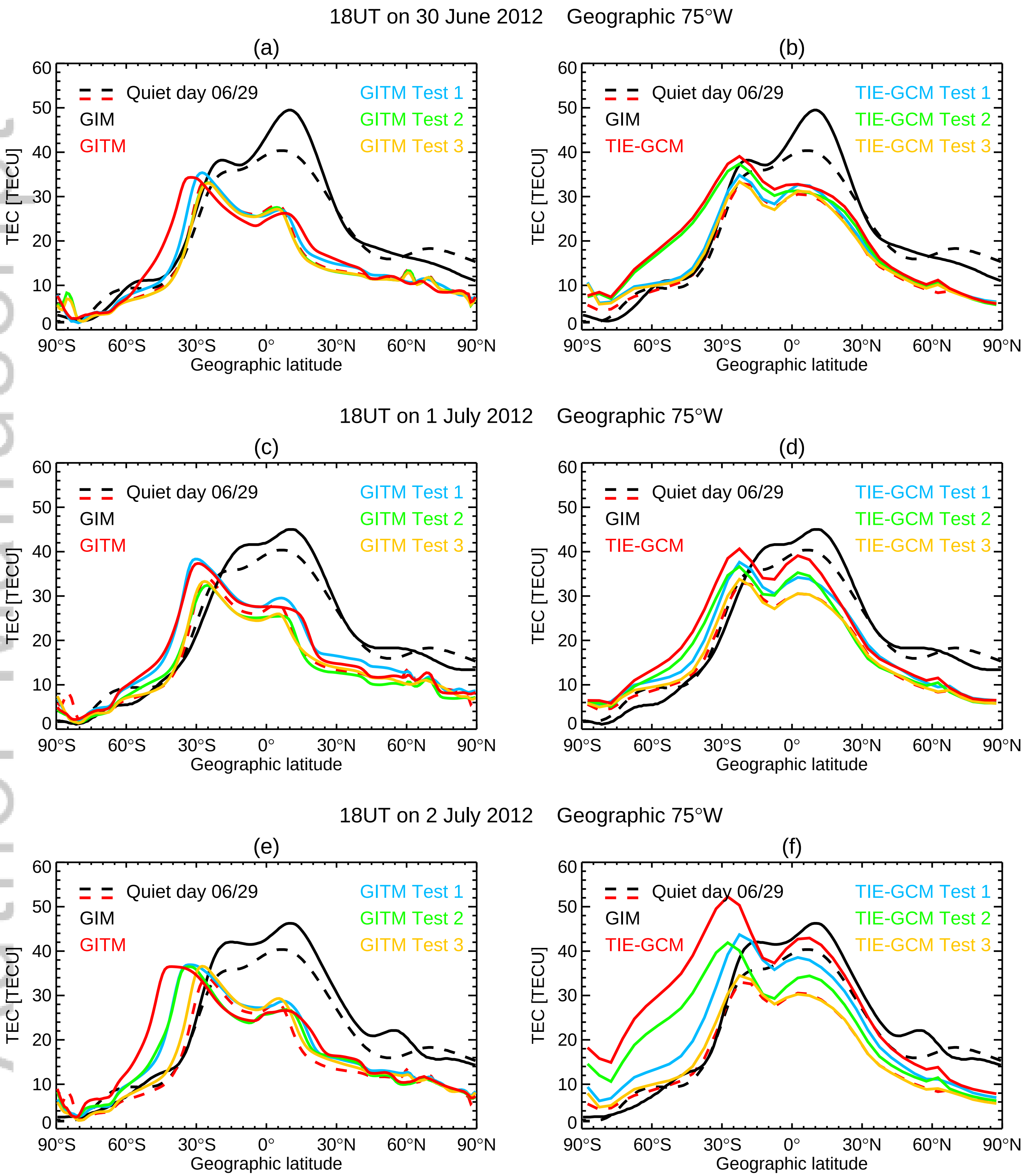
18UT on 30 June 2012 Geographic 75°W
(a)
(b)
Quiet day 06/29
GIM
GITM
GITM Test 1
GITM Test 2
GITM Test 3
TIE-GCM
TIE-GCM Test 1
TIE-GCM Test 2
TIE-GCM Test 3
TEC [TECU]
Geographic latitude
90°S
60°S
30°S
0°
30°N
60°N
90°N
18UT on 1 July 2012 Geographic 75°W
(c)
(d)
18UT on 2 July 2012 Geographic 75°W
(e)
(f)

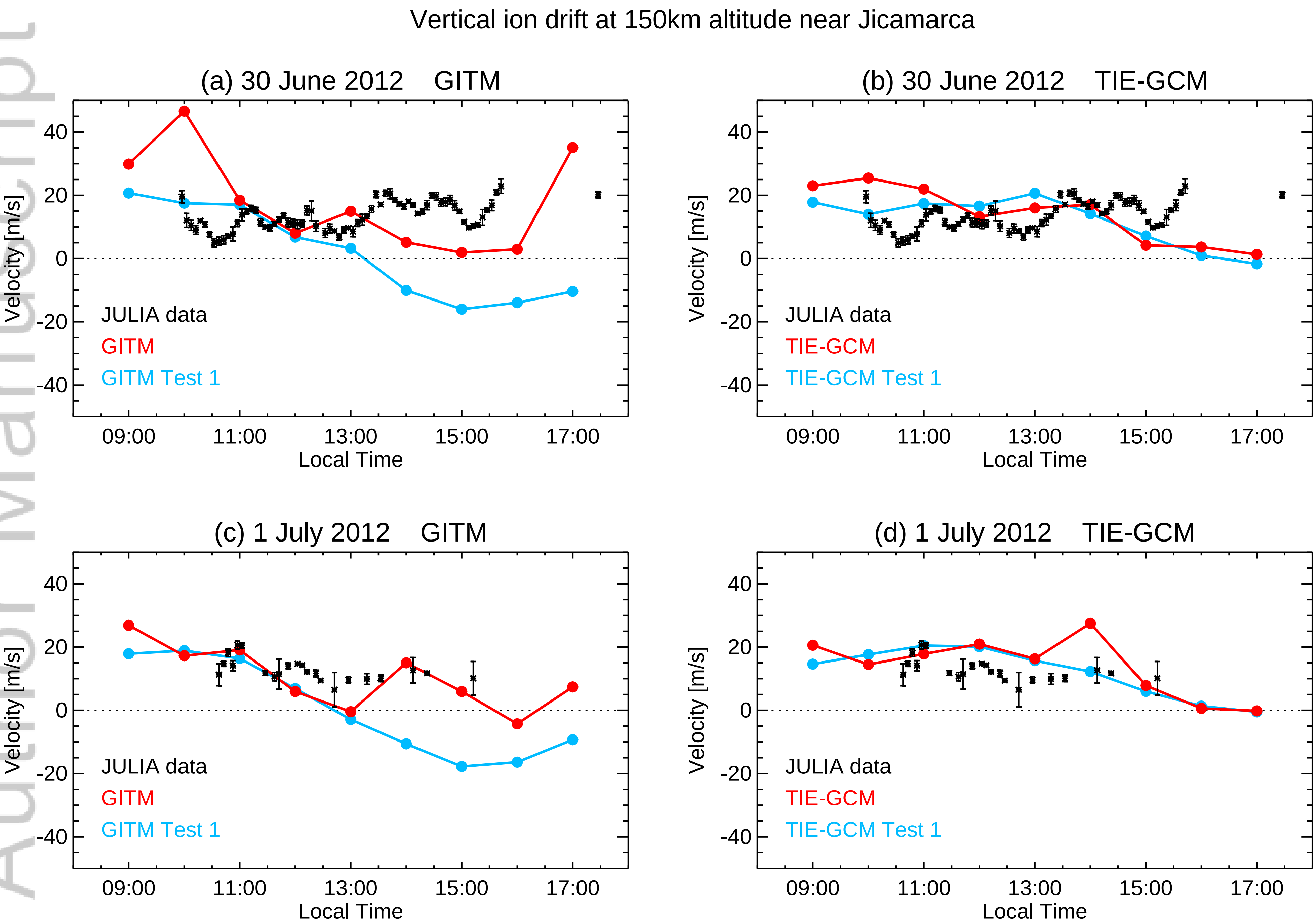

Vertical ion drift at 150km altitude near Jicamarca
(a) 30 June 2012 GITM
(b) 30 June 2012 TIE-GCM
(c) 1 July 2012 GITM
(d) 1 July 2012 TIE-GCM
Velocity [m/s]
Local Time
40
20
0
-20
-40
09:00
11:00
13:00
15:00
17:00
JULIA data
GITM
GITM Test 1
TIE-GCM
TIE-GCM Test 1

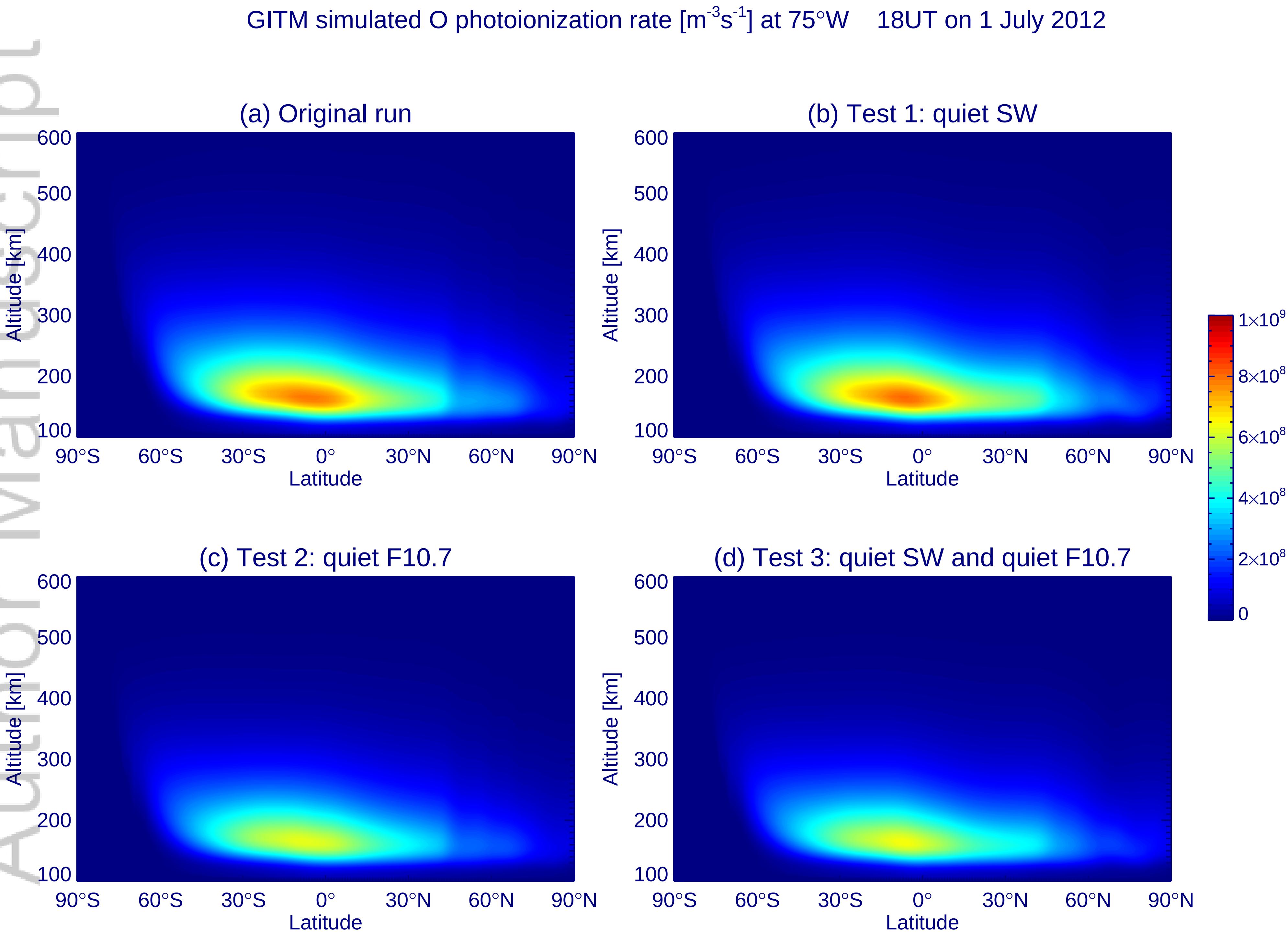

GITM simulated O photoionization rate [m-3s-1] at 75°W 18UT on 1 July 2012
(a) Original run
(b) Test 1: quiet SW
(c) Test 2: quiet F10.7
(d) Test 3: quiet SW and quiet F10.7
Altitude [km]
600
500
400
300
200
100
90°S
60°S
30°S
0°
30°N
60°N
90°N
Latitude
1×10^9
8×10^8
6×10^8
4×10^8
2×10^8
0

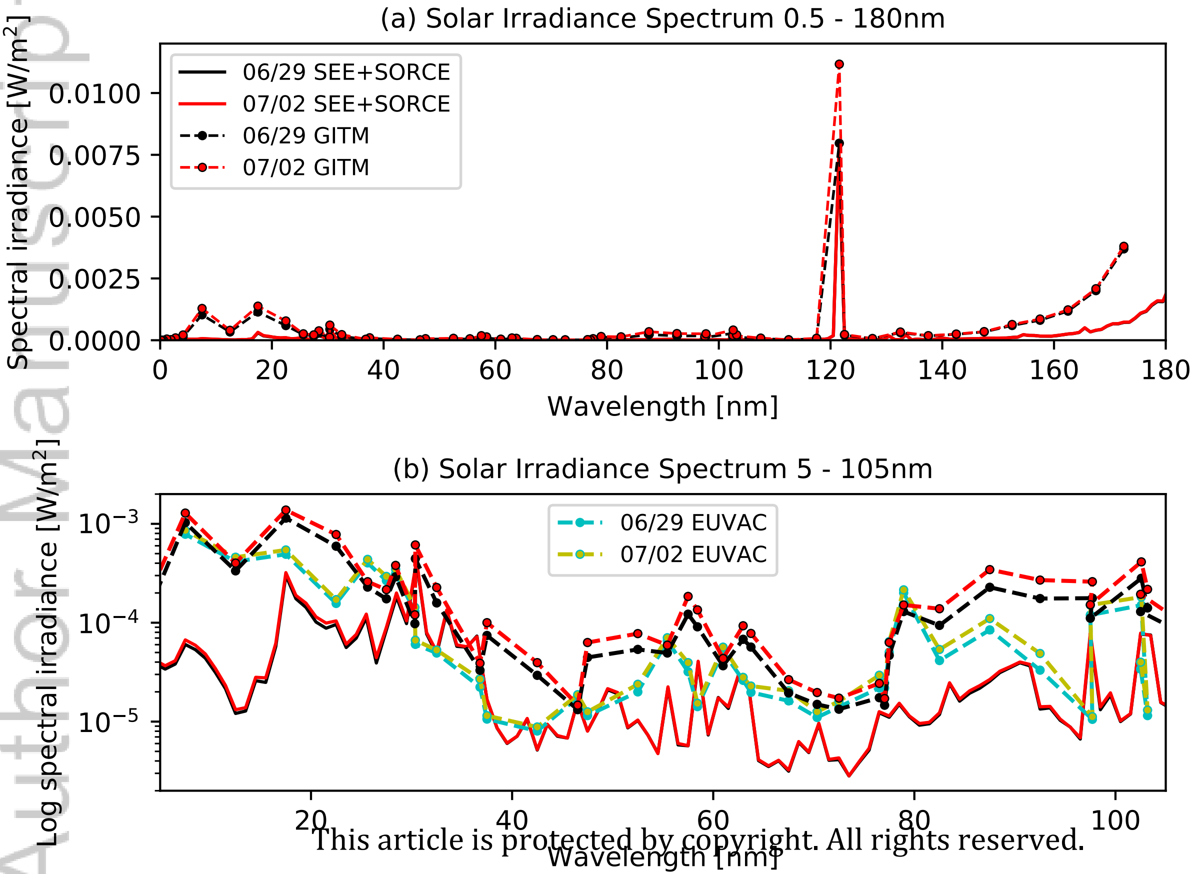
(a) Solar Irradiance Spectrum 0.5 - 180nm
06/29 SEE+SORCE
07/02 SEE+SORCE
06/29 GITM
07/02 GITM
Spectral irradiance [W/m^2]
0.0100
0.0075
0.0050
0.0025
0.0000
0
20
40
60
80
100
120
140
160
180
Wavelength [nm]
(b) Solar Irradiance Spectrum 5 - 105nm
06/29 EUVAC
07/02 EUVAC
Log spectral irradiance [W/m^2]
10^{-3}
10^{-4}
10^{-5}
20
40
60
80
100
Wavelength [nm]

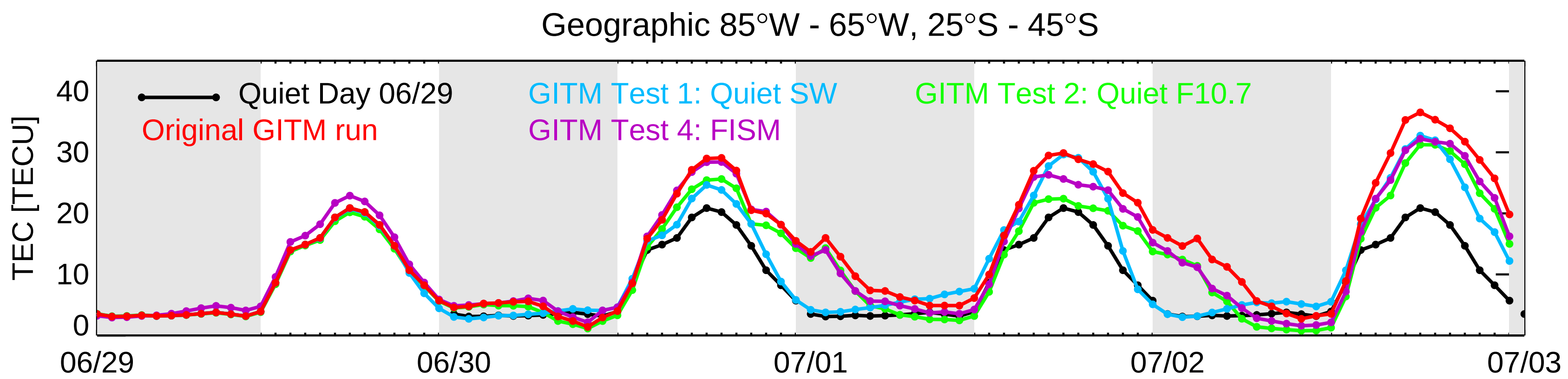
Geographic 85°W - 65°W, 25°S - 45°S
Quiet Day 06/29
Original GITM run
GITM Test 1: Quiet SW
GITM Test 4: FISM
GITM Test 2: Quiet F10.7
TEC [TECU]
40
30
20
10
0
06/29
06/30
07/01
07/02
07/03